Research Square

Preprints are preliminary reports that have not undergone peer review.
They should not be considered conclusive, used to inform clinical practice,
or referenced by the media as validated information.

# Glial metabolic states in human sporadic amyotrophic lateral sclerosis uncovered by spatial single-cell proteomics.

**Gen Ohtsuki**

ohtsuki.gen.7w@kyoto-u.ac.jp

Kyoto University https://orcid.org/0000-0003-3004-5886

**Momoka Hikosaka**

Kyoto University https://orcid.org/0000-0002-2314-3237

**Miyu Kinoshita**

Kyoto University

**Kumiko Uemura**

Kyoto University

**Md Shamim Hossain**

Rheology Institute of Functional Food

**Masako Abe**

Kyoto University

**Md Sorwer Alam Parvez**

University of Alabama at Birmingham https://orcid.org/0000-0002-9726-1009

**Siwakorn Punyawatthananukool**

Mahidol University

**Mari Yoshida**

Institute for Medical Science of Aging, Aichi Medical University https://orcid.org/0000-0002-8520-6184

**Tatsuaki Tsuruyama**

Kyoto University

**Article**

**Keywords:**

**Posted Date:** March 25th, 2026

**DOI:** https://doi.org/10.21203/rs.3.rs-9006017/v1

**License:** This work is licensed under a Creative Commons Attribution 4.0 International License.
Read Full License

**Additional Declarations:** There is **NO** Competing Interest.

# Glial metabolic states in human sporadic amyotrophic lateral sclerosis uncovered by spatial single-cell proteomics.

Momoka Hikosaka[1,9], Miyu Kinoshita[1,2,9], Kumiko Uemura[2,9], Md. Shamim Hossain[3,9], Masako Abe[4], Md Sorwer Alam Parvez[5], Siwakorn Punyawatthananukool[1,6], Mari Yoshida[7,*], Tatsuaki Tsuruyama[1,8,*], and Gen Ohtsuki[1,2,10,*]

[1] Department of Drug Discovery Medicine, Graduate School of Medicine, Kyoto University, Kyoto, Japan
[2] Department of Neuroscience, Graduate School of Medicine, Kyoto University, Kyoto, Japan
[3] Division of Lipid Cell Biology, Institute of Rheological Functions of Food, Fukuoka, Japan
[4] Division of Advanced Biomedicine, Medical Research Support Center, Graduate School of Medicine, Kyoto University, Kyoto, Japan
[5] Department of Psychiatry and Behavioral Neurobiology, Heersink School of Medicine, University of Alabama at Birmingham, Alabama, USA
[6] Department of Pharmacology, Faculty of Medicine Siriraj Hospital, Mahidol University, Bangkok, Thailand
[7] Department of Neuropathology, Institute for Medical Science of Aging, Aichi Medical University, Aichi, Japan
[8] Department of Clinical Laboratory, Kyoto Tachibana University, Kyoto, Japan
[9] These authors contributed equally.
[10] Lead Contact
*Correspondence: myoshida@aichi-med-u.ac.jp, tsuruyam@ddm.med.kyoto-u.ac.jp, and ohtsuki.gen.7w@kyoto-u.ac.jp

**Contact Info**
Gen Ohtsuki, Ph.D.
Tel: +81 (0)75 366 7477
ORCID: 0000-0003-3004-5886

**Abstract**

Sporadic amyotrophic lateral sclerosis (ALS) is characterized by selective motor neuron vulnerability accompanied by prominent glial responses, yet their molecular heterogeneity and spatial organization in the human central nervous system and spinal cord remain incompletely defined. Here, we delineate ALS-associated glial states in situ by spatially resolved, single-cell proteomic profiling of postmortem human sporadic ALS and non-neurological control tissues across the motor cortex, spinal cord, and cerebellum. We identify subpopulations of astrocytes and microglia co-expressing both canonical ALS markers together with newly implicated ALS-associated proteins, including phosphorylated TDP-43, UBQLN2, TREM2, IL6ST, and glutaminase (GLS). These glial states are consistent with transcriptomic signatures characterized by *TP53* and *GLS* upregulation, indicating convergence on senescence stress- and glutamine metabolism-related pathways. Notably, p53–GLS-associated profiles are selectively enriched in anatomically vulnerable regions in ALS, supporting region-specific glial metabolic alterations in human disease. Together, these findings provide insight into the metabolic alterations in ALS-affected human tissue and highlight the relevance of spatial context in shaping glial responses to neurodegeneration.

**Main text**

Amyotrophic lateral sclerosis (ALS) is a fatal neurological disease characterized by progressive loss of motor neurons in the spinal cord and motor cortex, including the precentral gyrus [1, 2]. ALS is typically adult onset (highest between ages 55 and 75), with variability in onset timing, site, and progression. Prevalence and incidence are higher in males than females [3]. While a subset of cases is linked to genetic mutations—most commonly a hexanucleotide repeat expansion in *C9orf72*—the majority of ALS cases are sporadic (sALS), particularly in East Asian populations where *C9orf72* expansions are rare [4]. Other genes associated with ALS include *SOD1*, *TARDBP*, and *FUS*, although many cases of ALS have no clear genetic cause. Environmental stress and lifestyle factors also influence the disease. A defining pathological feature is the mislocalization and aggregation of phosphorylated TDP-43 (pTDP-43), a nuclear RNA-binding protein encoded by *TARDBP*. Phosphorylation of TDP-43 disrupts its nuclear localization, leading to cytoplasmic aggregation [5] and preceding symptom onset [6]. Accompanied by ubiquilin 2 (UBQLN2) and optineurin, pTDP-43 accumulates in the cytoplasm of affected neurons and glial cells, forming ubiquitin-positive inclusions and impairing RNA processing, proteostasis, and cell viability. These aggregates, along with classic histological features such as acidophilic degeneration and basophilic inclusions, disrupt the normal function of neurons, causing their degeneration and pathological glial changes.

While neuronal degeneration is a hallmark of ALS, disease-associated glial assemblies initiated by inflammation are a key contributor to the progression of neurodegenerative diseases [7, 8]. Reactive microglia and their cytokine secretion induce cytotoxic disease-associated astrocytes [9], as observed in Alzheimer's disease, where both cell types cluster around amyloid-β plaques [8]. Inflammatory stress, oxidative damage, and lysosomal dysfunction converge to exacerbate protein misfolding and neuronal loss in neurological diseases, such as ALS, Alzheimer's disease, and Parkinson's disease [10, 11]. In ALS, comparable glial reactivity is implicated, while how distinct glial subtypes are spatially distributed across vulnerable regions of human CNS remains poorly resolved.

Additionally, eosinophilic degeneration and gliosis are typical pathophysiological findings in the neurodegenerative samples, yet the relevance is not sufficiently explored. Therefore, spatial proteomic profiling of ALS brains could be essential for understanding region-specific vulnerabilities.

Aberrant p53—a cellular senescent factor—activity has been implicated in ALS pathology, while its expression is typically low in the brain. A recent comprehensive analysis of human induced pluripotent stem cell-derived motor neurons (iPSMNs) demonstrated remarkable upregulation of p53 signaling in ALS, observed in both iPSMNs and post-mortem spinal cord tissue [12]. In p53-induced senescent cells, glutaminase (GLS), but not GLS2, is consistently upregulated, facilitating tissue fibrillization and cellular senescence [13]; nonetheless, the involvement of p53-glutaminase axis in ALS pathogenesis remains insufficiently defined. Glutamate toxicity has been recognized as a central mechanism in aging. Given that GLS expression is prominent in glial cells, including astrocytes, it may enhance glutamate production and amplify excitotoxic stress.

Despite extensive research on astrocytes in ALS [14–17], treatments based on SOD1-ALS mouse models have largely failed to translate into ALS therapies, highlighting the requirement for further investigation into reactive microglia- and astrocyte-mediated neurodegeneration in human tissues [15]. Moreover, ALS and frontotemporal lobar degeneration (FTLD) patients exhibit reduced levels of unsaturated phospholipids, cholesterol, and apolipoprotein, suggesting dysregulated lipid metabolism, too [18, 19]. These alterations may influence degeneration of motor neurons and survival time. Alternatively, autophagy and apoptosis are essential processes for maintaining cellular homeostasis. Autophagy clears damaged cytosolic proteins and organelles, while apoptosis eliminates compromised cells, leading to cell death. Aging-related decline in these systems may exacerbate neurodegeneration and contribute to disease progression [20]. However, it is now widely acknowledged that RNA expression at both tissue and single-cell levels does not consistently reflect corresponding protein expression, posing a significant challenge for the interpretation of

97 comprehensive transcriptomic data and its direct application to drug development and therapeutic
98 strategies. In this study, we integrate spatial proteomic profiling and histopathology to test multiple
99 hypotheses.

100 Since the discovery by Neumann et al. (2006) of ubiquitin-positive inclusions containing
101 hyperphosphorylated, ubiquitinated, and cleaved TDP-43 via metabolic disruption in ALS and FTLD
102 [21], cytoplasmic pTDP-43 inclusions have been observed across multiple CNS regions, often
103 alongside Bunina bodies in lower motor neurons [22]. TDP-43, a 411–amino-acid protein, harbors most
104 autosomal dominant mutations linked to familial ALS and FTLD within its C-terminal glycine-rich
105 domain, which contains RNA recognition motifs and mediates pathological protein interactions [23].
106 Misfolded TDP-43 forms filamentous, hyperphosphorylated aggregates that correlate with stress
107 granule (SG) assembly, caspase-3 activation, and neurodegeneration [24, 25]. SGs are stress-induced
108 cytoplasmic ribonucleoprotein assemblies formed via liquid–liquid phase separation of RNA-binding
109 proteins and untranslated mRNAs, leading to transient translational repression. Proteins such as
110 Ataxin-2 (ATXN2) and FUS are recruited to SGs and regulate their dynamics, and SG components
111 can be cleared via SQSTM1/p62-dependent autophagy. Impaired SG disassembly or proteasomal
112 function, as seen with mutant SOD1, promotes toxic and insoluble cytoplasmic aggregation [26] and is
113 implicated in motor neuron vulnerability of ALS and Alzheimer's disease. Emerging evidence also
114 suggests prion-like propagation of misfolded TDP-43 across brain regions [27–30], with downstream
115 cellular senescence, DNA damage, and metabolic dysregulation contributing to neurodegenerative
116 progression.
117
118 Collectively, ample evidence in ALS implicates protein misfolding [23, 24, 26, 27], aggregation [20,
119 21, 29], altered RNA processing [24, 25], oxidative stress [10, 11], and cellular senescence [7, 12], along with glial
120 and neuronal inflammation [7–10, 14, 15–17, 25]. Yet, few studies have simultaneously examined spatial
121 protein distribution and cell type specificity across multiple brain regions within human ALS tissue.

To fill this gap, we performed spatial proteomics to delineate pathophysiological alterations within distinct cellular compartments, integrating single-cell resolution, proteomic profiling, and histopathology in human samples. This approach enabled us to test the hypothesis that disruption of cellular metabolism and homeostasis, together with inflammatory signaling and glial phenotypic transitions, contributes to cell type-specific neurodegeneration during ALS progression

## Results

### Increased *TP53* and *GLS* expression in the ALS motor cortex single-cell transcriptome.

To define early molecular alterations in ALS, we analyzed single-cell transcriptomic profiles of the human neocortex [31]. Across neuronal and glial populations, global transcriptional suppression was evident particularly in L5 VAT1L+ and L3/5 SCN4B+ neurons [31]; however, astrocytes exhibited selective enrichment of TP53-regulated metabolic programs. We analyzed and reproduced upregulated and downregulated gene subsets from astrocytes, microglia, oligodendrocytes, oligodendrocyte precursor cells (OPCs), endothelial cells, excitatory neurons [L5/6 neurons], and inhibitory interneurons [somatostatin(+) and parvalbumin(+) neurons] in the motor cortex (Supplementary Figs. 1a, 1b, and 2), most of which showed reduced expression. Enrichment analysis using astrocyte-upregulated genes further revealed activation of *TP53*-regulated metabolic genes (mitochondrial oxidative phosphorylation and respiratory chain function, particularly in the regulation and activity of cytochrome c oxidase (Complex IV) and cellular redox homeostasis), and neuronal structural integrity and calcium-dependent signal transduction pathways (Supplementary Fig. 1c and 1d). Using an alternative platform, gene set enrichment analysis (GSEA) also indicated the involvement of *TP53_REGULATES_METABOLIC_GENES* and *TRANSMISSION_ACROSS_CHEMICAL_SYNAPSES*, including upregulation of *GLS*

(Supplementary Fig. 3). These data suggest a p53-associated metabolic shift in astrocytes as a prominent early transcriptional signature in ALS (Supplementary Fig. 1e).

*TP53* encodes the p53 protein, which had been reported to activate GLS2 in cancer cells [32]. GLS2 is also a p53-inducible regulator of glutamine metabolism and reactive oxygen species [33]. We then compared the gene expression of *GLS*, *GLS2*, *TP53*, and *c-MYC* in the same public dataset and found that both *GLS2* and *TP53* were significantly increased in astrocytes of ALS patients, while there are many cells below detection (Supplementary Fig. 1f). *GLS* transcript exhibited a significant increase in ALS astrocytes and microglia compared to pathologically negative (PN) samples (ALS vs. PN) (Supplementary Fig. 1f), indicating enhanced *GLS* expression in ALS glia. A previous key study on senescence showed an increase in *GLS* expression in p53-induced senescent fibroblasts [13]. Given the elevated GLS protein levels in ALS brain or spinal cord tissues, GLS(+) cell populations and ALS-marker protein expression likely localize to areas with ALS lesions. Other cell types, including L5/6 pyramidal neurons and OPC showed significant increases in both *GLS*, *GLS2*, and *TP53* in ALS compared to PN, while inhibitory interneurons, oligodendrocytes, and endothelial cells did not (Supplementary Fig. 2). Additionally, there were no significant differences at RNA levels between females and males (Supplementary Fig. 1g), consistent with findings in other neurodegenerative diseases [34]. These analyses suggested the presence of ALS-specific senescent cell populations and GLS-mediated glutaminolysis changes in ALS pathology.

**Spatial proteomics of postmortem human ALS brains.**

Spatial proteomic analysis of human brain samples from the precentral gyrus, anterior horn of the lumbar spinal cord, and cerebellar cortex enabled mapping of region-specific protein distributions and assessment of pathological correlations. Samples were collected from 12 participants (6 sALS patients and 6 age-matched non-ALS controls (AC); 71.2 ± 2.4 years for sALS and 62.2 ± 8.7 years for AC [mean ± SD]) through Aichi Medical University Brain Resource Center (Supplementary Table 1). Clinical phenotyping of participants is tabulated in Supplementary Tables 2 & 3. Formalin-

fixed, paraffin-embedded (FFPE) tissues were analyzed via imaging mass cytometry (IMC) using Hyperion™ system (Standard Biotools). Individual regions of interest (ROIs) selected for IMC are shown in Supplementary Fig. 4. We applied IMC to comprehensively map the spatial distribution of multiple ALS-associated factors at the single-cell resolution (Fig. 1a, b). Following optimization of metal-conjugated antibody panels (Supplementary Fig. 5a), we performed single-cell segmentation, clustering, and spatial analyses on tissues from different brain regions. After quality control filtering (Methods; Supplementary Methods), 75,332 high-quality single-nucleus spatial profiles were retained for downstream analysis across samples and regions (Supplementary Fig. 5a, b; Methods). Translationally distinct cell populations were annotated and classified into neuronal, glial, and immune cell lineages based on marker protein expression patterns (Fig. 1c-e). A summary of cellular composition in the precentral gyrus across all participants is shown in Supplementary Fig. 5b and Supplementary Table 1. Channel-separated and magnification images of IMC are shown in Supplementary Fig. 6. Based on known marker expression, we identified in precentral gyrus: 2,515 astrocytes (20.6%), 858 microglia (7.0%), 4,300 excitatory neurons (35.3%), 736 inhibitory neurons (6.0%), and 3,772 other cell types (31.0%), which likely include oligodendrocytes and vascular cells (Fig. 1f-h and Supplementary Table 4). All findings were reproducible across donors, sexes, and disease statuses (Supplementary Fig. 5c, d). Annotation in the spinal cord and cerebellum was also done as in Fig. 1i-k and 1l-n, respectively.

**ALS-associated cell transition and co-localization of subpopulations with pathological signatures in the precentral gyrus.**

First, in the gray matter of the precentral gyrus (Supplementary Fig. 7a-e), we compared the expression levels of differentially expressed proteins (DEPs) other than those used for the initial annotation (Fig. 2a). We identified highly expressed proteins of ALS markers, including pTDP-43, FUS, ATXN2, UBQLN2, and APOE across various cell types. FUS and APOE expression were pronounced in neurons. Thus, as is widely known in ALS, upregulation of pTDP-43 and UBQLN2

was confirmed. Remarkably, we observed a significant increase in GLS and IL6ST in ALS, suggesting promoted glutaminolysis and an IL6-related inflammation. TREM2 (triggering receptor expressed on myeloid cells 2) showed a significant increase in astrocytes, immune cells, neurons, and another population, indicating expression by different cell types in ALS motor cortical tissues or aged brains. Meanwhile, there were no differences in SQSTM1, CH24H (cholesterol 24S-hydroxylase or CYP46A1), and ORF1 between ALS and AC, suggesting less relevance to selective markers for autophagy, CH24H-related brain cholesterol homeostasis, and LINE-1 (Long interspersed element-1) retrotransposons. TANK-binding kinase 1 (TBK1) and pTBK1 were not significantly altered.

To further investigate cell types in the classified cell population, we reclassified astrocytic cells into five subpopulations, Iba1(+) microglial cells into three subpopulations, and excitatory cells into five subpopulations (Fig. 2b, c). We defined ALS-associated cell states in astrocytes, immune cells, and excitatory neurons from marker expression (pTDP-43, UBQLN2, GLS, and TREM2) (Fig. 2c). Cell transition analysis using trajectory reconstruction for their interplay and possible differentiation suggested differences between astrocyte subclusters with low ALS-marker expression (Astro_3 and Astro_4) and ALS-oriented astrocyte subcluster 1 (Astro_1) (Fig. 2d). Astro_1, immune cell subcluster 1+3 (Immune_1+3), and the pTDP-43-accumulated neuron subcluster 4 (Excit_4) were highly ALS-marker positive, indicating distinct subpopulations with ALS-marker protein expression (Fig. 2e). In the white matter, cell clusters highly expressing ALS markers were also implicated (Supplementary Fig. 7f-j). Given the interactions among astrocytes, microglia, and degenerated neurons in ALS pathophysiology, the spatial distribution of their subclusters may contribute to the manifestation of ALS-related tissue pathology (Fig. 2f). We analyzed the pairwise distances between each cell in the subclusters (astrocytes, Iba1(+) immune cells, and pTDP-43-accumulated neurons) and compared the cell distributions within 240 μm [8]. Distance analysis of closely localized cells revealed significant clustering between subpopulations, such as between

Astro_1, Immune_1+3, and Excit_4, using bootstrap validation (Fig. 2g; see Methods). Finally, we confirmed the pathological changes associated with these subcluster distributions in serial hematoxylin and eosin (H&E) histological stained sections (Fig. 2h). Indeed, localized disruptions in the gray matter were observed, including perivascular damage with gliosis, apparent detachment of neural tissue from perivascular regions, and eosinophilic neuronal degeneration, as demonstrated in H&E-stained sections (Figs. 2i-k and 4a-c). These regions exhibited subpopulations expressing ALS-associated markers, accompanied by focal neuronal damage, neurodegeneration, immune cell accumulation, possible blood-brain barrier dysfunction, and the presence of gliotic fibrils. Single-cell transcriptome data of sALS motor cortex also revealed signatures of astrocytic gliosis potentially driven by TGFβ signaling, which is regulated by p53, as well as chronic inflammatory signaling via IL6 (Supplementary Fig. 8a). Concurrently, lysosome-related gene dynamics suggest enhanced autophagy and mitophagy, which supports the notion that cellular homeostasis is disrupted through lysosomal membrane permeabilization and acidification (Supplementary Fig. 8b).

**ALS-associated changes in the lumbar spinal cord and cerebellar cortex.**

The spinal anterior horn is a well-known region of neurodegeneration in ALS patients. We compared the expression levels of DEP between ALS and AC (Fig. 3a and Supplementary Fig. 9). In ALS samples, we found highly expressed proteins, including pTDP-43, ATXN2, UBQLN2, APOE, GLS, IL6ST, and TREM2 across cell types. Next, we subclassified spinal cord cell types identified in our single-cell dataset. Astrocytic cells were divided into six subpopulations, immune cells into three, and neurons into five (Fig. 3b, c), among which astrocyte subcluster 6 (Astro_6), immune cell subcluster 3 (Immune_3), and neuron subcluster 5 (Neuron_5) were identified as disease-oriented (Fig. 3c, d). We further analyzed the pairwise distances of cells within these subclusters (astrocytes, immune cells, and pTDP-43 accumulated neurons) and the neighborhood cell distribution, which revealed significantly closer spatial allocations between Astro_6, Immune_3, and Neuron_5 (Fig. 3e, f). Lastly, the H&E-stained section exhibited histological evidence of neurodegeneration, confirming

the ALS-involved pathology in the spinal anterior horn (Figs. 3g-i and 4d, e). These results suggest that the regions exhibiting ALS pathological features correspond to the area containing ALS-associated subclusters across cell types in the anterior horn of the spinal cord.

Although the cerebellum is not classically regarded as a primary site of neurodegeneration or pTDP-43 pathology in ALS, its contribution to motor dysfunction has been proposed [35]. We therefore performed spatial proteomic analysis of cerebellar samples from patients with ALS and age-matched controls. In contrast to the precentral gyrus and spinal cord, DEPs in the cerebellum did not display distinct global expression patterns (Supplementary Fig. 10). Increases in ALS-associated markers such as pTDP-43 and ATXN2 were not uniformly increased across cell types. However, UBQLN2 and APOE were broadly elevated, whereas GLS upregulation was restricted to excitatory neurons, largely corresponding to granule cells and an unidentified cell population. Although SQSTM1 expression was unchanged, the selective enrichment of UBQLN2 and GLS suggests the presence of discrete ALS-associated cellular subpopulations within the cerebellum (Supplementary Fig. 10).

Comparing male and female samples, transcriptomic analysis revealed no significant sex differences (Supplementary Fig. 1g); however, proteomic analysis showed elevated pTDP-43 in female astrocytes and microglia across all brain regions, while GLS expression was higher in male astrocytes and microglia (Supplementary Fig. 11d, h, and l). These findings suggest sex-dependent differences between transcript and protein expression, supporting greater female resilience to the neurological disease (*see also* Xu et al. (2020) [3]).

**p53 and GLS co-localize in pTDP-43 accumulating cells and a hypothetical framework.**

The localization of proteins implicated in ALS pathogenesis was assessed by immunofluorescence staining in human samples. We first qualitatively examined the co-expression of pTDP-43, GLS, GLS2, and p53 in microglia, astrocytes, neurons, and oligodendrocytes, identified by Iba1(+), GFAP(+), NeuN(+), and Olig2(+), respectively (Supplementary Fig. 12). We also occasionally used transmitted-light images and DAPI staining for assisting neuronal identification. The semi-

quantitative scores indicate a greater frequency of co-localization of ALS-associated molecules (Supplementary Fig. 12). Next, we quantified fluorescence intensity in Iba1(+), GFAP(+), NeuN(+), and Olig2(+) cells in ALS and AC immunofluorescence (IF) samples (Fig. 5a and b). Two-way ANOVA with multiple comparisons, following normalization to AC and stratification by pTDP-43(+) and pTDP-43(–) cells, revealed that GLS and p53 are highly expressed in pTDP-43(+) astrocytes, microglia, and neurons in ALS samples of both the precentral gyrus and spinal cord, as well as GLS2 partially (Fig. 5a and b). Furthermore, super-resolution images in Fig. 5c demonstrate co-localization of pTDP-43 aggregates and GLS within the cytosol of an ALS GFAP(+) astrocyte, but not nucleus. Co-localization of p53 and GLS, and expression of GLS2 in a pTDP-43-positive astrocyte are shown in Fig. 5d. In a representative neuron with pTDP-43 deposition, clear accumulation of GLS is observed (Fig. 5d). Another image of Iba1(+) microglia in the spinal cord also shows co-expression of pTDP-43 and GLS (Fig. 5e), consistent with the cell-type-resolved proteomic profiles identified by IMC.

To examine downstream effects of TDP-43 pathology, we analyzed *TP53* signaling using a publicly available sALS dataset [31]. Positive regulators of p53, including *ATM* and *CHEK2*, were upregulated in ALS compared with PN, whereas negative regulators, *SNAI2* and *DLX2*, showed no significant changes (Supplementary Fig. 13a, b). Downstream effectors of p53 involved in the DNA damage response (DDR) and apoptosis—PUMA, NRF2, BAX, and p21, encoded by *BBC3*, *NFE2L2*, *BAX*, and *CDKN1A*—were also elevated (Supplementary Fig. 13c), consistent with DDR and p53 pathway activation. Notably, NRF2, encoded by *NFE2L2*, previously implicated in metabolic regulation, has been linked to GLS expression [37], suggesting that nuclear TDP-43-loss-associated DDR and p53 activation may contribute to subsequent GLS upregulation (Supplementary Fig. 13f). Both ribotoxic stress response-related transcripts, *MAP3K20*, *MAPK14*, and *11*, and integrated stress response-related transcripts, *EIF2AK4* and *EIF2A*, were elevated via cytosolic pTDP-43-associated stress (Supplementary Fig. 13d, e). Collectively, these results indicate a

mechanistic cascade in ALS from TDP-43 abnormalities through DDR/p53 activation to metabolic stress and GLS elevation, bypassed with cytosolic RNA damage responses (Supplementary Fig. 13f).

## Discussion

pTDP-43 aggregation, pathological signatures, and neuronal degeneration are characteristic of sALS [1–5]. Leveraging publicly available single-cell transcriptome data [31], this study applied IMC to perform single-cell spatial proteomics analysis on brain tissues from sALS patients and age-matched non-ALS participants. Strikingly, our proteomic analysis uncovered highly distinct expression patterns in astrocytic and microglial clusters in sALS tissues, exhibiting inflammatory ALS-associated glial features. These subpopulations spatially overlapped with histopathological characterizations, revealing the p53-GLS axis as a consistent molecular signature of disease-associated ALS pathology.

In this study, single-cell proteomic analysis using IMC revealed ALS-associated cell populations in ALS tissues, spatially confined to areas of gliosis and eosinophilic neuronal degeneration (Figs. 2-4). Notably, in neuropathology, neuronal acidophilicity on H&E staining does not necessarily reflect intracellular metabolic acidification. It is commonly observed in the terminal-stage LMNs of ALS, as well as in ischemia or circulatory disturbances. Conversely, even in mitochondrial diseases such as MELAS, cells do not uniformly exhibit acidophilicity. These considerations suggest that the association between ALS-associated glial populations and acidophilic neurons likely reflects degenerative stress, protein denaturation, and ribonucleic loss, rather than simple metabolic acidification or lysosomal alterations, supporting a role for complex metabolic-inflammatory interactions in ALS-affected regions.

Complementarily, single-cell transcriptomic profiling indicated upregulation of *TP53* and *GLS* in astrocytes and microglia, whereas *MYC* were not substantially expressed (Supplementary Fig. 1f), and p53-associated genes involved in glutamate metabolism and the DDR were upregulated (Supplementary Fig. 13a-c, and f). The convergence of these transcriptomic and proteomic findings

led us to propose a model in which a p53-GLS metabolic axis is a defining feature of this pathogenic glial state. While our human tissue data cannot establish causality, they provide the first *in situ* evidence that this axis is a relevant molecular signature of human ALS pathology. Consistently, single-cell proteomic analysis using IMC demonstrated high expression of GLS in the precentral gyrus and spinal cord anterior horn, corresponding to regions with pathological findings (Figs. 2 and 3). These findings support the involvement of glutaminolysis. GLS is an amidohydrolase enzyme that synthesizes glutamate from glutamine, a process essential for normal glutamatergic presynaptic release in neurons. Provided GLS expression is elevated in astrocytes, glutamine may be diverted from neuronal synaptic terminals and instead drive glutamate transmission from glia [38]. Therefore, high GLS expression in astrocytes may accelerate glutamatergic gliotransmission and indirect propagation in ALS motor cortex (Supplementary Fig. 14). Since excessive glutamate should damage neurons via excitotoxicity, homeostatic regulatory mechanisms and glutamate transport reduction in the brain are likely to be involved [39, 40].

We identified glial alterations in both astrocytes and microglia. Distinct clusters expressing pTDP-43, UBQLN2, TREM2, IL6ST, APOE, and GLS were tightly localized in the precentral gyrus and spinal cord, with no marked alterations in the cerebellum despite elevated UBQLN2 expression. In astrocytes, we found the ALS-associated cluster belonged to a GFAP-low population (Supplementary Discussion, *inset* Figures 1*A* and 1*B*), correlating with the RNA levels (Supplementary Discussion, *inset* Figure 1*C*) [31]. Neurotoxic astrocytes can be induced by microglia-derived inflammatory signals in both mouse and human systems [9]. C3-positive reactive astrocytes have been observed not only in ALS but also in Alzheimer's and Parkinson’s diseases.

Although disease-associated microglia are characterized by *TREM2* expression, we found that TREM2 protein was not predominantly expressed in microglia but rather in other cell types in the human ALS motor cortex and spinal cord (Figs. 2 and 3). TREM2 is primarily expressed on microglia as a surface receptor, and its soluble form has been shown to ameliorate pathological

features in experimental models of Alzheimer's disease [41]. Therapeutic activation of TREM2 using engineered agonistic antibodies has been proposed as a neuroprotective strategy since mutations in the *TREM2* gene were identified as a risk factor. Its efficacy has been evaluated in preclinical models and early-phase clinical trials [42, 43], without serious adverse events reported during short-term evaluation [43]. However, our findings show that in the human ALS motor cortex and spinal cord, TREM2 protein was not predominantly restricted to microglia but was also detected in other cell types (Figs. 1-3). These observations suggest that defining disease-associated microglia solely by TREM2 expression may oversimplify the cellular landscape in ALS. Indeed, even within microglia, TREM2-positive populations are heterogeneous and may include both neuroprotective and neurotoxic subgroups. Moreover, the identity and functional significance of TREM2-expressing non-microglial cells in aged human tissue remain incompletely characterized. Given that microglial replacement has shown beneficial effects in mouse models of neurodegeneration and psychiatric disorders [44–46], our results raise the possibility that TREM2-targeted or microglia-directed therapies may have broader or cell-type–specific effects in ALS than previously anticipated. Further comprehensive studies using aged human samples are warranted to clarify glial heterogeneity and to refine therapeutic strategies targeting TREM2-related pathways across neurodegenerative diseases.

Tissue regions enriched in pTDP-43-associated cellular clusters exhibited eosinophilic neuronal degeneration. Although murine studies have implicated links between neural activity, glutamate dysregulation, and neurodegeneration [47-49], the precise contribution of glutamate-mediated excitotoxicity to human ALS pathophysiology remains incompletely understood (Supplementary Fig. 14). Our multi-omics analyses raise the possibility that nuclear TDP-loss may contribute to genomic instability and DNA damage response pathways, engaging p53-depending metabolic state change for glutamate production. Such alterations could influence neuronal and glial activity via excess glutamate release. In turn, activity-dependent shifts in TDP-43 localization have been described [47], suggesting a potential contribution to nuclear TDP-43-loss and cytosolic pTDP-43 aggregation

within a feedback loop that depends on cell- and neuron-type specificity (Supplementary Fig. 13f and 14).

Additionally, Bunina bodies were observed in regions of the lumbar spinal cord enriched for pTDP-43–positive cells, in keeping with classical ALS histopathology (Fig. 4d) [50]. These inclusions may reflect underlying proteostatic stress, rather than a specific organelle dysfunction. Prominent gliosis in ALS-cluster rich area (Figs. 2i and 4b, c) may be associated with stress-responsive pathways, including p53- and TGF-β-related mechanisms, accompanied by vimentin upregulation (Supplementary Fig. 8a). Notably, the GLS inhibitor BPTES has been reported to mitigate p53-induced fibroblast senescence phenotypes [13], suggesting that modulation of glutamine metabolism may influence stress-related cellular states. GLS and GLS2 regulation appear to be cell type-, region-, and disease stage-dependent (Fig. 5a, b). Complementary IF analyses further indicated distinct cell type specific co-expression patterns in glia and neurons (Fig. 5c-e).

Low-complexity domains can promote β-sheet assembly and crystallization of TDP-43, processes linked to mitochondrial stress, RIPK-mediated necroptosis, and activation of innate immune pathways, including cGAS-STING [51, 52]. Although STING classically signals through the TBK1–IRF3 axis, TBK1 can also cooperate with optineurin to regulate autophagy and endolysosomal trafficking. Multiplex imaging of ALS tissues revealed significant changes in TBK1 and pTBK1 expression in spinal cord astrocytes and other cell types. Concomitantly, IL6ST signaling was elevated in astrocytes and neuronal populations in both motor cortex and spinal cord (Figs. 2 and 3). These findings suggest a role for coordinated TBK1- and IL6R–IL6ST-dependent signaling in glial inflammatory responses in ALS neurodegeneration, accompanied by transcriptomic signatures indicative of JAK–STAT pathway activation (Supplementary Fig. 8a).

Overall, our findings provide fundamental insights into the unique assembly states of ALS-associated glia and identify GLS positivity with chronic inflammation in human samples, corresponding to characteristic histopathological features. Transcriptomic analysis further

demonstrated *TP53* and *GLS* upregulation in sALS; however, several limitations of this study should be noted. First, our findings are based on a postmortem cohort of Japanese ALS cases, which substantially lacked *C9orf72* mutations and therefore represent an understudied population [4]. Consistent with our observations, elevated p53 expression and activity have been reported in postmortem CNS tissues from patients with ALS, as well as in other neurodegenerative conditions, including Alzheimer's disease [53, 54], Parkinson's disease [55], and Huntington's disease [56]. Early neuropathological studies similarly documented increased nuclear p53 immunoreactivity in neuronal and glial populations of the motor cortex and spinal ventral horn of ALS cases [57, 58]. Maor-Nof et al. (2021) showed that neurons expressing *C9orf72*-derived dipeptide repeats activate a p53-centered transcriptional program that drives neurodegeneration via p53-upregulated modulator of apoptosis (PUMA) [59]. PUMA acts downstream of both p53-dependent and -independent apoptotic pathways. Suppressing p53 mitigates neuronal and axonal degeneration in mouse, fly, and patient-derived iPSC models, highlighting a transcription-dependent mechanism. Collectively, these findings support a broader role for p53 activation in both *C9orf72*-mediated and sporadic neurodegenerative diseases. Second, while IMC allows spatially resolved protein profiling in long-preserved specimens−where protein expression remains relatively stable compared with RNA—the Hyperion® platform restricts the number of available antibodies that could be analyzed simultaneously. Due to the constraint, we were unable to directly assess oligodendrocyte alterations or to comprehensively profile diverse immune cell subtypes. We further acknowledge that antibody-based spatial profiling of human postmortem tissue carries inherent technical limitations, including variability in signal intensity and the use of adjacent sections for orthogonal validation. Our conclusions therefore rely on reproducible spatial patterns observed across multiple cases rather than on absolute signal intensity from individual markers, with further details provided in the Supplementary Discussion and Methods sections. Third, although our data offer cellular-level spatial information and reveal distinct localization of ALS-associated clusters, its spatial resolution limits finer subclassification and

organelle-scale observations. Super-resolution techniques support these observations (Fig. 5) and are expected to further advance understanding of human nanostructural biology. Cytosolic aggregation of pTDP-43 may contribute to ribosomal stress and RNA damage responses (Supplementary Fig. 13d-f) [27, 60]. Despite these constraints, our study underscores spatial proteomics as a powerful approach to uncover glial heterogeneity and regional vulnerability in human neurodegeneration (Supplementary Fig. 14).

## Methods

### *Study design*

The objectives of this study were (i) to characterize distinct cellular populations expressing ALS-associated proteins in brain and spinal postmortem samples from patients with sALS and age-matched control volunteers, (ii) to identify possible differences in glutaminase expression and the involvement of inflammation among senescent human tissues, and (iii) to determine if histopathological findings of ALS tissues corroborate with the spatial localization of disease-specific cellular cluster features. For human spatial proteomics, we conducted IMC to analyze protein expression patterns in ALS-characteristic brain regions, including the precentral gyrus and spinal cord anterior horn, comparing differences by sex and MCI status. For fine structure investigation, we conducted immunofluorescence imaging using confocal and super-resolution microscopies. This prospective case-control study focused on a Japanese population and did not include screening for C9orf72 repeat expansions. Such expansions are rare in Japanese individuals, accounting for approximately 3% of familial ALS cases and fewer than 0.5% of sporadic ALS cases [4].

### *ALS patients and participants without ALS*

All participants were informed of the study's content, procedures, and objectives, and provided written informed consent prior to enrollment. The study was conducted in accordance with the Aichi Medical University Brain Resource Center guidelines for observational research, covering both implementation and analysis phases. The human sample size was determined based on the design of previous studies. Participants were randomly selected from those whose brain and spinal cord tissues were adequately collected and well preserved. FFPE-fixed human brain samples from each patient with ALS and participant without ALS pathology (aged control, i.e., AC) were obtained at Aichi Medical University Brain Resource Center via Japan Brain Bank Net. We followed rigorous neuropathological criteria when diagnosing and confirming each case of ALS/FTLD-TDP and age-related pathology (Supplementary Fig. 5b). All procedures for human postmortem subject use were in accordance with the Declaration of Helsinki, and the study protocol was approved by the Ethics Committee of the Aichi Medical University and the Ethics Committee of Kyoto University Graduate School of Medicine (R4048). Patient information is provided in Supplementary Table 1. Clinical phenotyping and neuropathological findings of participants are tabulated in Supplementary Tables 2 & 3. All IMC data were collected and subsequently filtered based on predefined inclusion and exclusion criteria, which are described in detail below. To optimize the concentration of metal-conjugated antibodies, we initially performed IMC on samples from one sALS patient and one age-matched control. All other data were included in the analysis, provided that tissue staining and IMC acquisition met quality standards. Data quality control, sampling, analysis criteria, and replication were all appropriately conducted. Criteria for the analysis of public single-cell datasets are also described below.

### *Imaging mass cytometry*

#### *Tissue staining*

The staining procedure for tissue imaging for the Hyperion® imaging system (Standard BioTools) followed standard immunohistochemistry and immunofluorescence (IF) protocols for tissue collection, tissue processing, and staining. Imaging mass cytometry (IMC) was performed as described previously [46] with minor modifications for human brain and spinal cord tissues. Postmortem samples were obtained from patients with ALS and non-ALS control participants who, based on clinical data and treatment history, had no diagnosed motor or cognitive impairments in life. These samples were used for both IMC, hematoxylin and eosin (H&E) staining, and IF experiments. After perfusion and fixation with 10% formalin, brains were kept in formalin for two days at 4°C. Then, brain tissues were dehydrated, degreased, and embedded in paraffin. Paraffin-

embedded tissue blocks were sectioned by 4-μm thickness, attached to a glass slide, and dried at 37°C for 24 hours. We took brain samples from the precentral gyrus, the anterior horn of lumbar spinal cord, and the cerebellar cortex of 12 participants (6 ALS patients and 6 aged non-ALS controls). After stretching paraffin with a slide-oven, sections were dewaxed in fresh xylene for 20 min (FUJIFILM Wako Pure Chemical Co., Osaka, Japan), and the slides were hydrated in descending grades of ethanol for deparaffinization. After incubation with antigen retrieval solution (Antigen Retrieval Reagent pH 9.0 (10x), S236784-2 Agilent® for precentral gyrus and cerebellum; Citrate Buffer, pH 6.0, 10x, Antigen Retriever, C9999 Sigma-Aldrich for spinal cord) and immersion with 3% BSA (Bovine Serum Albumin, A3059, Sigma-Aldrich) blocking solution, the slides were placed in a hydration chamber, and the antibody master mix was applied onto the section enclosed with a PAP pen. Instead of using sterile water, we used Maxpar Water and Maxpar PBS (Standard BioTools: 201069 and 201058, respectively) to prevent contamination of a very small amount of metal ingredients. Tissues on the slides were incubated overnight with the antibody cocktail at 4°C in a hydration chamber. Afterward, slides were washed in 0.2% Triton X-100 in Maxpar PBS and Maxpar PBS. Lastly, for nuclear staining, the tissues were stained with Intercalator-Ir (Cell-ID™ Intercalator-Ir, Standard BioTools: 201192A) in Maxpar PBS (80 μL/section of 1:400 diluted solution) for 30 min at room temperature in a hydration chamber.

The antibody cocktail was custom-designed for this study's aim and composed of antibodies shown in Supplementary Fig. 1a; the detailed version of tissue staining method is described in Supplementary Methods.

We selected the antibodies listed above to visualize various cell types: neurons (NeuN, MAP2), inhibitory neurons (GAD67), cholinergic neurons (ChAT), astrocytes and the blood-brain barrier (GFAP, AQP4), microglia (IBA1, CX3CR1, TMEM119), antigen-presenting cells (MHC class II), helper T cells (CD4), cytotoxic T cells (CD8), and regulatory T cells (FoxP3). To assess cellular function, we used TREM2 as a marker for disease-associated cell states. For ALS-specific markers, we used pTDP-43, FUS, ATXN2, and UBQLN2. TDP-43, an RNA-binding protein, serves as the non-phosphorylated counterpart of pTDP-43. APOE was used to examine lipid metabolism; p62/SQSTM1, a ubiquitin-binding protein, served as a marker for autophagosome cargo; and glutaminase (GLS) was used as a marker for glutamine metabolism. We also assessed ORF1 (LINE-1), a retrotransposable element; CH24H (CYP46A1), involved in cholesterol metabolism; and IL6ST (gp130, CD130), an inflammatory cytokine signal transducer. Phosphorylated TBK1 (Ser172) is involved in IκB kinase (IKK) and NF-κB signaling, while TBK1 more broadly is associated with cell proliferation, apoptosis, autophagy, autoimmunity, and anti-tumor immunity. Finally, PD-1, PD-L1, and PD-L2 were included to investigate immune checkpoint pathways. We conducted pilot staining using one aged control (N = 1) and one ALS case (N = 1) to determine the optimal concentrations of metal-conjugated antibodies for IMC. For each brain region, we tested three different antibody concentrations and two antigen retrieval conditions. Note that the antibody concentrations recommended by manufacturers for immunohistochemistry may not be directly applicable to IMC, making rigorous quality control essential.

We manually conjugated each antibody to lanthanide (Ln) metals using Maxpar® X8 Antibody Labeling Kit (Standard BioTools), following the Maxpar Antibody Labeling User Guide (PRD002 Rev 17, Chapter 3: Maxpar X8 Antibody Labeling Kits). Briefly, the Ln metal solution was loaded onto Maxpar X8 polymer, and the antibodies were partially reduced with TCEP [Tris(2-carboxyethyl)phosphine hydrochloride (TCEP) solution, pH 7.0, 646547, Sigma-Aldrich]. Both the Ln-loaded polymer and the reduced antibody were conjugated as described previously [46]. The detailed version of tissue staining method is described in Supplementary Methods.

The final concentration of metal-conjugated antibodies are 141Pr-AQP4, 10 μg/ml; 143Nd-p62/SQSTM1, 15 μg/ml; 145Nd-UBQLN2, 20 μg/ml; 147Sm-Glutaminase, 15 μg/ml; 149Sm-NeuN, 25 μg/ml; 150Nd-PD-L1, 6 μg/ml; 151Eu-MAP2, 24 μg/ml; 152Sm-ATXN2, 15 μg/ml; 153Eu-ORF1 (LINE-1), 20 μg/ml; 154Sm-pTDP-43, 25 μg/ml; 155Gd-FoxP3, 6 μg/ml; 156Gd-CH24H,

17.5 μg/ml; 158Gd-GFAP, 30 μg/ml; 159Tb-IL-6ST, 15 μg/ml; 160Gd-IBA1, 20 μg/ml; 161Dy-CX3CR1, 6.9 μg/ml; 162Dy-pTBK1 (Ser172), 17.72 μg/ml; 163Dy-CD4, 3.5 μg/ml; 164Dy-TMEM119, 20 μg/ml; 165Ho-PD-1, 5 μg/ml; 166Er-GAD67, 20 μg/ml; 167Er-CD8, 3.5 μg/ml; 168Er-FUS, 10 μg/ml; 169Tm-ChAT, 25 μg/ml; 170Er-APOE, 10 μg/ml; 171Yb-TREM2, 20 μg/ml; 172Yb-PD-L2, 6 μg/ml; 174Yb-MHC class II, 10 μg/ml; 175Lu-TDP-43, 20 μg/ml; 176Yb-TBK1, 15 μg/ml. We determined the final concentration of metal-conjugated antibodies from the IMC image of one experiment across the brain (precentral gyrus, spinal cord, and cerebellum) by conducting the IMC imaging with three different concentrations of metal-conjugated antibodies and different retrieval conditions (pH 9.0 or 6.0), as mentioned above. While we have not directly tested the metal-labeled antibody in our study, previous reports have shown that antibodies labeled under similar conditions retain their antigen-binding activity [46], and we confirmed the IMC signals during optimization following the manufacturer's methodological recommendations.

***Imaging acquisition***

The brain-tissue samples and the slides were first taken the image using a smartphone camera to reference the regions of interest (ROIs) prior to IMC image acquisition. For IMC analysis of the precentral gyrus, ROIs were selected to span from the superficial to the deeper layers of the neocortex, focusing on areas in which the vertical cortical architecture was well preserved. The selected ROIs encompassed layers II/III through layer V or deeper, where Betz cells exist, thereby capturing the principal laminar organization relevant to motor cortical pathology. In the lumbar spinal cord, ROIs were chosen from either the right or left anterior (ventral) horn in the anterior portion of the cord. These ROIs covered nearly the entire gray matter region, including Rexed lamina IX (column IX), which contains α-motor neurons. Although pathological changes typically initiate in the cervical spinal cord, we focused on the L3–L4 lumbar segments to assess residual neurons at a later disease stage. For the cerebellum, ROIs were selected from the hemispheric region.

Using the Hyperion® imaging system (Standard BioTools), we initially selected three to four relatively large ROIs (~2 mm × 3 mm) arbitrarily from each section. After adjusting the imaging region of the sample slide using the reference image, we acquired images of one to three individual ROIs (maximum size: 1500 μm × 1576 μm) at 1-μm resolution, noting that it takes around 3.5 hours for imaging a 1.5 mm × 1.5 mm region. We subsequently analyzed the data from ROIs exhibiting the highest signal quality. For one precentral gyrus sample and one spinal cord sample, datasets were acquired twice; for all other samples, a single dataset was used. The Hyperion® system retrieves signals from 30 metal-tagged antibody channels, along with the two nuclear markers Ir191 and Ir193, which correspond to the Cell-ID™ Intercalator-Ir signals. Acquired IMC images were saved as a separate MathCad (.mcd) files. The MCD Viewer software (v1.0.560.6) visualized the mcd-files as images and exported them in OME-TIFF 16-bit format.

***Cell segmentation and clustering***

The cell segmentation and clustering were performed following a previously reported protocol [46]. Briefly, individual tiff images per antibody marker were exported using MCD Viewer. Nuclear images for Ir191 and Ir193 were imported into Cell Profiler v4.2.1 to obtain the cell mask. Next, we added the nuclei signal of Ir191 and Ir193 with the "ImageMath" module. Then, we used the "IdentifyPrimaryObject" module for the nuclei segmentation, setting the typical diameter of the objects from a minimum of 4–8 pixels to a maximum of 30–50 pixels, depending on the brain region. The segmented nuclei were expanded by 1–4 pixels using the Distance-N method to identify the whole-cell objects. We converted the cell objects into images using "ConvertObjectToImage" and saved the image masking the cells. The histoCAT-analysis provides clustering at the single-cell level. The cell mask along with corresponding tiff images was loaded into the histoCAT v1.76 and generated the single-cell data. Images with uneven staining or insufficient signal intensity were excluded from further analysis. Cells with signal acquisition errors in any marker were removed from the dataset. Of note, Cell-ID™ Intercalator-Ir signals do not always indicate the nuclei position

in samples where DNA has leaked from the DNA membrane into the cytosol, probably due to fixation conditions or specimen preservation. This issue was particularly evident in the relatively large neurons in old spinal cord samples. Therefore, we newly developed a programming code to semi-manually select the IMC multidimensional data and to omit the data located redundantly in the large cell body neurons and reselected the appropriate nucleus signal (Supplementary Discussion, *inset* Figure 2). Signal noise detected in the spinal cord white matter was also excluded from further analysis.

Downstream analyses were performed primarily using the Seurat package in R. Data were processed separately for each brain region. We identified 12,181, 7,956, 16,343, and 38,852 cells from precentral gyrus gray matter, white matter, spinal cord, and cerebellum, respectively. Within each region, all data were scaled using the ScaleData() function and merged into a single Seurat object. Technical runs from the same sample were merged after assigning unique run identifiers. Highly variable proteins were identified using the FindVariableFeatures. From this set, immune checkpoint- and activation-related markers (PD-1, PD-L1, PD-L2, TREM2, and MHC class II) were excluded in precentral gyrus gray matter and spinal cord, and principal component analysis (PCA) was performed using the remaining variable proteins with the RunPCA() function. Prior to clustering, batch-effect correction was applied using Harmony with both sample identity and technical run specified as batch variables within each brain region (9 datasets for precentral gyrus gray matter, 9 datasets for precentral gyrus white matter, 11 datasets for the spinal cord, and 10 datasets for the cerebellum). We generated a primary cluster using the FindClusters() function (Fig. 1c-e). Based on marker expression profiles and spatial distribution, clusters were classified as astrocyte, Iba1(+) immune cell, excitatory neuron, inhibitory neuron, or cells of other identity. Note that inhibitory neurons include ChAT(+) neurons. In the spinal cord and precentral gyrus white matter, excitatory and inhibitory neurons were difficult to distinguish and therefore labeled as "Neuron". Clusters of cells were visualized using UMAP, and the number of cells per cell type is summarized in Supplementary Table 4. For Fig. 1f, i, and l, protein expression values for each marker were averaged per cell type and Z-score-scaled per marker. The resulting matrix was visualized as a heatmap. Color values represent the Z-scored average expression level of each marker in each cell type.

Marker expression levels across cell types were compared by calculating effect sizes according to the formula: = (Mean $_{ALS}$ – Mean $_{AC}$) / pooled standard deviation. Statistical significance was assessed using the Wilcoxon signed-rank test, and p-values were adjusted for multiple hypothesis testing using the false discovery rate (FDR) method (Fig. 2a, 3a, and Supplementary Fig. 10f).

We performed reclustering analysis for each cell type, excluding the other cluster (Fig. 2b, 3b, and Supplementary Fig. 10g). The number of cells in individual subclusters (excluding the other cluster) ranged N = 91–512 in ALS and N = 114–580 in AC across 15 clusters in the precentral gyrus gray matter (Fig. 2b, and Supplementary Fig. 7a-c), N = 92–617 in ALS and N = 136–533 in AC across 9 clusters in the precentral gyrus white matter (Supplementary Fig. 7f-h), N = 67–656 in ALS and N = 133–1,109 in AC across 14 clusters in the spinal cord (Fig. 3b and Supplementary Fig. 9a-c), N = 147–5,231 in ALS and N = 147–6,396 in AC across 10 clusters in the cerebellum (Supplementary Fig. 10a-c and 10g). In Fig. 2c and 3c, differentially expressed proteins (DEPs) across subclassified cell types were visualized using dot plots. For each marker (pTDP-43, GLS, UBQLN2, and TREM2), IMC signal values were extracted from the reclustered dataset. Color scales represent normalized expression levels, where IMC signal intensities were Z-score–standardized across all cells within each cell type (astrocytes, immune cells, and neurons). Z-scaling was performed independently for each marker to allow relative comparison of expression patterns across subclassified clusters. Circle sizes indicate mean expression value for each marker within a given cell type was defined as 100%, and the average expression values of each subcluster were represented proportionally relative to this reference. To quantify disease-associated expression

patterns (Fig. 2c and 3c, *bottom*), protein expression values for four markers (pTDP-43, GLS, UBQLN2, and TREM2) were Z-score–standardized across all cells in each cell type. To avoid negative values introduced by standardization, the Z-scored matrix was shifted 3σ by adding +3 to all values, and any remaining negative values were set to zero. For each cell, an integrated expression score was calculated as Euclidean distance^2 (the sum of squared normalized marker values) and visualized by mean-value heatmap. The subcluster with the highest integrated expression score is highlighted in turquoise. For trajectory analysis (Fig. 2d), astrocytes from ALS samples were extracted and reanalyzed using Monocle 3 package (v1.3.7). UMAP embeddings computed by Monocle were visualized by coloring cells according to Seurat-defined subclusters or pseudotime values. The pseudotime root was defined as the centroid of the astrocyte subcluster 4 (Astro_4), which showed the lowest expression of differentially expressed markers (Fig. 2c), and cellular state transitions were inferred relative to this starting point.

***Spatial distance analysis***

For the cell-cell pairwise distance analysis (Fig. 2g and 3f), we measured the Euclidean distances between cell pairs across clusters, as described previously [46], with minor modifications. After classifying single cells, we extracted astrocyte, microglia, and pTDP-43-high neuron clusters for analysis. We then computed pairwise distances between cells from different clusters within a 200-240 μm radius and obtained *q*-values based on distances distribution. Clusters were considered spatially close if at least one pairwise distance between them was significantly different from those of other cluster pairs. To assess whether such differences occurred by chance, we performed a bootstrap procedure followed by a two-sample Kolmogorov-Smirnov (KS) test. We created a randomized dataset by merging the two clusters and shuffling the cell labels. We generated a new distance matrix within the same range from this randomized dataset. We then compared this randomized distance matrix with the original using the two-sample KS test at a significance level of 0.03 (precentral gyrus) and 0.05 (spinal cord). If the randomized distance matrix was significantly smaller than the original, this indicated that the observed spatial clustering might have occurred by chance. This process was repeated 2,000 times to estimate the false positive rate. We considered the difference statistically significant when the error rate was below 0.03 in the precentral gyrus and below 0.005 in the spinal cord across 2,000 iterations. Note that parameters were adjusted depending on the cell numbers.

***H&E staining***

Serial sections used for IMC were stained with hematoxylin and eosin (H&E).

***Image acquisition and analysis of H&E-stained samples***

H&E-stained images were acquired using a virtual slide scanner (NanoZoomer S60, Hamamatsu Photonics) and a DP73 microscope camera (Olympus) mounted on an Olympus BX53 microscope. Microscopic images were captured using UPlanSApo 40X /0.95 NA or UplanSApo 100X /1.40 NA oil-immersion objective lenses, and image processing was performed with cellSens Standard software (Olympus). We performed quantitative analysis of neuronal acidity using scanned images and ImageJ. Neurons were randomly selected within the ALS-associated cluster-rich and ALS-associated cluster-poor areas of the H&E-stained sections from ALS patient tissues, as well as from AC samples, corresponding to the IMC observation areas. We manually extracted the cell body, excluding the nucleus, and calculated the mean RGB values. Neuronal acidity was quantified based on the difference between the red (R) and blue (B) channel intensities after subtracting the green (G) channel intensity. Color tone analysis of the H&E-stained sections indicated a greater eosinophilic trend in the red-shifted neurons used for image quantification. A total of 240 neurons from the precentral gyrus (Fig. 2j and 2k) and 96 neurons from the spinal cord (Fig. 3g and 3h) were analyzed.

***Immunofluorescent Staining***

***Tissue staining***

Given the distinct staining chemistry of metal-tagged antibodies used in IMC, we additionally assessed subcellular localization using conventional IF across different cell types. Paraffin-embedded 4-μm tissue sections from the precentral gyrus and spinal cord (2 ALS patients and 2 aged non-ALS controls) were prepared in the same manner as for IMC. Sections were stretched using a slide oven, dewaxed in fresh xylene for 20 min (FUJIFILM Wako Pure Chemical Co.), rehydrated in a series of ethanol solutions of descending concentration, and rinsed in water. Antigen was retrieved with citrate-based antigen retrieval solution (pH 6.0; Antigen Retriever C9999, Sigma-Aldrich; or Sodium Citrate Antigen Retrieval Buffer (50X), Proteintech) by microwave heating at 650 W for up to 5 min. After cooling to room temperature, sections were washed in Milli-Q water, PBS, and 0.1%Triton X-100 in PBS for 10 min each. Sections were circled with a PAP pen and blocked with 3% bovine serum albumin (BSA; A3059, Sigma-Aldrich). Slides were placed in a humidified chamber, and primary antibodies were applied onto the tissue sections. We used the following primary, fluorescent probe-conjugated, and secondary antibodies for immunostaining: Alexa Fluor® 647 Anti-Iba1 antibody [EPR16588] (Abcam, Cat. No. ab225261; Rabbit Monoclonal; dilution 1/100), GFAP (GA5) Mouse mAb (Alexa Fluor® 647 Conjugate) #3657 (Cell Signaling Technology, Cat. No. 3657, RRID: AB_10693037; Mouse Monoclonal; dilution 1/50), Alexa Fluor® 647 Anti-NeuN antibody [EPR12763] - Neuronal Marker (Abcam, Cat. No. ab190565, RRID: AB_2732785; Rabbit Monoclonal; dilution 1/50), Olig2 (E6G6Q) XP® Rabbit mAb (Alexa Fluor® 647 Conjugate) #43829 (Cell Signaling Technology, Cat. No. 43829; Rabbit Monoclonal; dilution 1/50), Anti TDP-43, phospho Ser409/410 (Cosmo Bio Co., Ltd., Cat. No. TIP-PTD-M01A, RRID: AB_3695645; Mouse Monoclonal; dilution 1/2500), P53 Monoclonal antibody (Proteintech, Cat. No. 60283-2-Ig, RRID: AB_2881401; Mouse Monoclonal; dilution 1/100), Glutaminase-1/GLS1 (E4T9Q) Rabbit mAb (BSA and Azide Free) #84021 (Cell Signaling Technology, Cat. No. 84021; Rabbit Monoclonal; dilution 1/100), GLS2 Polyclonal antibody (Proteintech, Cat. No. 20171-1-AP, RRID: AB_3085600; Rabbit Polyclonal; dilution 1/100), Anti-p53 antibody [E26] (Abcam, Cat. No. ab32389, RRID: AB_776981; Rabbit Monoclonal; dilution 1/1000), Donkey Anti-Mouse IgG H&L (Alexa Fluor® 488) (Abcam, Cat. No. ab150105, RRID: AB_2732856; Donkey Secondary antibody; dilution 1/500), Donkey Anti-Rabbit IgG H&L (Alexa Fluor® 555) (Abcam, Cat. No. ab150074, RRID: AB_2636997; Donkey Secondary antibody; dilution 1/500). Sequential immunofluorescent staining was performed in the following order at 4°C. Sections were incubated overnight with mouse primary antibodies against phospho-TDP-43 (Ser409/410) or p53, followed by incubation with Alexa Fluor® 488-conjugated anti-mouse secondary antibody for 2 h, and then incubated overnight with rabbit primary antibodies against GLS1, GLS2, or p53, followed by incubation with Alexa Fluor® 555-conjugated anti-rabbit secondary antibody for 2 h. Overnight incubation was performed with fluorophore-conjugated Alexa Fluor® 647 antibodies against GFAP, Iba1, NeuN, or Olig2. After immunostaining, sections were treated with TrueBlack® Lipofuscin Autofluorescence Quencher (Biotium) for 5 min to reduce autofluorescence, followed by nuclei staining with DAPI (1:1000 in PBS; Nacalai Tesque) for 10 min. And then, samples were mounted with VECTASHIELD® Mounting Medium (H-1000, Vector Lab) and coverslipped.

***Image acquisition***

Fluorescence images were acquired using an Olympus FV3000 confocal laser-scanning microscope equipped with a UPLSAPO 30XS oil-immersion objective (NA 1.05). Excitation wavelengths of 405, 488, 555, and 647 nm were used, and emitted fluorescence was collected using band-pass filters of 430–470, 500–530, 580–610, and 670–770 nm, respectively. Transmitted light images were acquired in parallel for morphological reference. Selected samples were additionally imaged using a Zeiss LSM 880 inverted confocal microscope (AxioObserver) equipped with an Airyscan detector and a Plan-Apochromat 40×/1.4 NA oil-immersion objective (DIC M27) to acquire super-resolution images with an approximate lateral resolution of 110–140 nm. Fluorescence excitation was performed using 405, 488, 561, and 633 nm laser lines. Emission signals were detected using Airyscan detectors in Super-Resolution mode with detection ranges of 450 nm, 523 nm, 595 nm, and

654 nm, respectively. Pinhole settings ranged from 1.95 to 2.83 Airy units, and images were acquired in frame scan mode with a scan zoom of 2.5-3, unidirectional scanning, and no frame averaging. Z-stack images were collected with a z-step size of 0.3-0.5 μm, comprising 7-12 optical sections over a total depth of 4 μm. Airyscan image reconstruction was performed using the Airyscan processing module in Zeiss ZEN software. Transmitted light images were also acquired. Z-stack images were processed in ImageJ/Fiji to generate maximum intensity projections (Fig. 5c-e).

***Analysis***

Confocal IF images were subjected to semi-quantitative analysis in the precentral gyrus and spinal cord (Supplementary Fig. 12a, b). Raw .oir files were imported into Fiji for analysis. Three fluorescence channels (488, 555, and 647) were overlaid and compared. Co-expression of pTDP-43, GLS, GLS2, and p53 was assessed within Iba1(+), GFAP(+), NeuN(+), and Olig2(+) cells, corresponding to microglia, astrocytes, neurons, and oligodendrocytes, respectively. Channel correspondence and signal overlap were examined across two to six independent experiments. The frequency of clearly superimposed IF signals per cell was independently evaluated by three investigators. Based on these assessments, co-expression rates were calculated and scored as follows: −, 0–10%; +, 10–40%; ++, 40–70%; and +++, 70–100%.

Next, IF signal intensities were quantified and averaged using a custom MATLAB script (Fig. 5a, b). In the precentral gyrus and spinal cord of ALS and AC samples analyzed by IMC, IF intensities of GLS, GLS2, and p53 were measured across six to ten ROIs within Iba1(+), GFAP(+), NeuN(+), and Olig2(+) cells, stratified by pTDP-43 positivity or negativity. IF signals from both pTDP-43(+) and pTDP-43(−) ROIs in AC samples were normalized to 1. Data are presented as box plots with individual data points in Fig. 5a and 5b, and statistical significance was assessed by two-way ANOVA (ALS vs. AC & pTDP-43(+) vs. pTDP-43(−)) on GLS, GLS2, and p53 signals, individually.

***Published scRNA-seq data analysis***

Raw count matrices were obtained from the Gene Expression Omnibus (GEO; accession number GSE174332) [31], comprising human motor cortex (BA4) samples from individuals with sporadic ALS (n = 17; 8 males and 9 females) and PN controls (n = 16; 8 males and 8 females). Cell type annotations were adopted from the original publication. Neuronal populations were grouped into excitatory and inhibitory classes, while non-neuronal populations were analyzed separately. Specifically, neuronal subtypes included layer 5/6 excitatory neurons (L5/6), parvalbumin (PV)-positive interneurons, and somatostatin (SOM)-positive interneurons. Non-neuronal subtypes included microglia, astrocytes, oligodendrocytes, endothelial cells, and oligodendrocyte precursor cells (OPC). Downstream analyses were performed in R using the Seurat package. Cells with more than 10% mitochondrial gene expression were excluded. We adopted a stricter threshold compared to the original work [31]. The data were log-normalized and subjected to principal component analysis (PCA). Batch effects were corrected using Harmony, with sample identity included as a covariate. Clustering was performed using the FindClusters() function at a resolution of 0.3, following nearest-neighbor identification via the FindNeighbors() function. Marker genes for each cluster were defined as the top 20 or 40 differentially expressed genes (DEGs), identified using FindAllMarkers().

For heatmap visualization, cell type-specific differential expression analysis was performed using donor-level pseudo-bulk RNA-seq data. Within each annotated cell type, genes were ranked based on adjusted p-values (Benjamini–Hochberg FDR), with $\log_2$ fold change used as a secondary criterion to prioritize biologically meaningful differences. The top 20 upregulated and top 20 downregulated genes with valid gene symbols were selected for visualization. Heatmaps were generated using logCPM expression values that were row-scaled (Z-score normalized) to emphasize relative expression patterns across donors for astrocytes and microglia (Supplementary Fig. 1a and b), as well as across all annotated cell types (Supplementary Fig. 2). To enhance visualization,

extreme values were capped. For enrichment analysis, we adopted Enrichr and applied top 40 upregulated genes using Reactome Pathways 2024 (Supplementary Fig. 1c and 1d). Expression levels of four genes of interest (*GLS*, *GLS2*, *TP53*, and *MYC*) were assessed across annotated cell types (Supplementary Figs. 1f and 2). In addition, expression levels of p53-related genes (*ATM*, *CHEK2*, *SNAI2*, *DLX2*, *BBC3*, *NFE2L2*, *BAX*, and *CDKN1A*) and RNA damage response-related genes (*MAP3K20*, *MAPK14*, *MAPK11*, *MAPK8*, *MAPK9*, *MAPK10*, *EIF2AK4*, and *EIF2A*) were evaluated in astrocytes and microglia, respectively (Supplementary Fig. 13a-e). For violin plots in Supplementary Figs 1f, 1g, 2, and 13a-e, cells lacking detectable expression of the gene of interest were excluded. Cluster-specific DEGs between ALS and PN groups were identified using the Wilcoxon rank-sum test, with FDR correction applied to p-values. Genes with zero expression across all cells were excluded from testing. Sex-specific expression analyses were conducted separately for astrocyte and microglia clusters, comparing ALS and PN groups within male and female donors.

For an alternative analysis of gene enrichment, we performed gene set enrichment analysis (GSEA) in Supplementary Fig. 3. The gene sets obtained as described above were analyzed using GSEA with the following parameters: gene set database, c2.cp.reactome.v2024.1.Hs.symbols; number of permutations, 1,000; enrichment statistic, classic; and ranking metric, log2_Ratio_of_Classes. We classified cells into distinct cell types, but one dataset was excluded due to the absence of astrocyte subgroups. Another dataset with a postmortem interval (PMI) exceeding 24 hours was omitted to minimize the inclusion of RNA-degraded samples.

For dot plots in Supplementary Fig. 8, color intensity represents the $\log_2$ fold change (ALS versus PN) calculated from normalized expression values within each cell type, where genes with zero expression across all cells were excluded from analysis. Dot size indicates the percentage of cells expressing the gene.

***Statistics***

Statistical analyses, including mean values, standard error of the mean (SEM), and *p* values, were performed using R (RStudio) and MATLAB (MathWorks). IMC and single-cell RNA-seq data are presented as box plots with whiskers or violin plots showing all data points and overlaid with mean ± SEM. For histopathological analyses, data are shown as bar graphs (mean ± SEM). Statistical significance between two groups was evaluated using two-tailed Wilcoxon rank-sum test or Kolmogorov-Smirnov (KS) test. For comparisons involving more than two groups, one-way ANOVA and two-way ANOVA followed by Tukey-Kramer or Bonferroni *post hoc* tests was performed. The spatial distribution of ALS-associated cell subpopulations in IMC images was estimated based on false positive rates using a two-sample KS test with randomized populations across multiple iterations. Statistical thresholds for significance are provided in the figure legends and methods. FDR corrections were applied for RNA-seq analyses. Exact sample size and replication are presented in Supplementary Data.

## Data availability

The IMC proteomics data have been deposited in Zenodo (an open-access repository developed under the European OpenAIRE program and operated by CERN) under accession number DOI: 10.5281/zenodo.18823151. All human data were de-identified prior to analysis, and no personally identifiable information is included in this study. All other data supporting the findings of this study are available within the Article and its Supplementary Information, or from the corresponding author upon reasonable request, subject to ethics committee restrictions. Source data are provided with this paper.

## Code availability

Custom R and Matlab codes for analyses in this study are available and will be shared upon request.

## Ethics & Inclusion Statement

This study was conducted entirely in Japan using human postmortem tissues obtained from the Aichi Medical University Brain Resource Center via Japan Brain Bank Net. All stages of the research process—including study design, tissue procurement, data generation, analysis, and manuscript preparation—were performed by researchers affiliated with Japanese institutions. No cross-border collaboration or transfer of biological materials occurred. All contributors who met authorship criteria were included as co-authors. Roles and responsibilities were discussed among collaborators prior to data analysis and manuscript preparation. No external local collaborators were excluded. The research addresses ALS, a condition of clinical relevance in Japan. Study approval was obtained from the Ethics Committee of Aichi Medical University and the Ethics Committee of Kyoto University Graduate School of Medicine (Kyoto University Hospital; approval number R4048). No biological materials were transferred outside Japan, and no benefit-sharing agreements were required. The study does not involve vulnerable populations, nor does it introduce stigmatization, discrimination, or personal risk to participants. All data were de-identified to ensure confidentiality. Relevant Japanese and international literature was considered and cited where appropriate.

**Acknowledgements**

We express our sincere gratitude to the donors and their families for generously providing the specimen, which was essential for this study. We thank the researchers and participants involved in Pineda et al. (2024) for granting permission to use their data. We appreciate Prof. Ryosuke Takahashi (Kyoto University Graduate School of Medicine), Prof. Shuh Narumiya and Prof. Masatoshi Hagiwara (Kyoto University Graduate School of Medicine, Department of Drug Discovery Medicine), and Prof. Tadashi Isa (Kyoto University Graduate School of Medicine, Department of Neuroscience) for their invaluable comments and support of the research. We thank Prof. Takehiko Fujino (Institute of Rheology Functions of Food) for his invaluable support of the research. We thank Dr. Suthinee Attachaipanich for helpful discussions during the early stages of this study. We thank S. Hiro, K. Sakano, and M. Fujii for their assistance. We also appreciate Sumitomo Pharma Co., Ltd., ONO PHARMACEUTICAL CO., LTD., Mitsubishi Tanabe Pharma Corporation, and KYORIN Pharmaceutical Co., Ltd., as the sponsors for the Department of Drug Discovery Medicine. We thank Dr. Kyoko Yoshikawa and Dr. Ken Fujimura (Takeda Pharmaceutical Company Limited) for the collaborative suggestions and invaluable comments.

Funding sources that supported this project include the Takeda Pharmaceutical Company Limited grant (GO), Takeda Science Foundation (GO), Japan Agency for Medical Research and Development (AMED) JP24gm6910013 (GO), Japan Agency for Medical Research and Development (AMED) JP24zf0127010 (GO), Japan Agency for Medical Research and Development (AMED) JP21wm0425019 (MY), and JSPS WISE program “The Graduate Program for Medical Innovation (MIP)” (MH).

**Author contributions**

The funders had no role in the study design, data collection, data analysis, decision to publish, or preparation of the manuscript. Conceptualization, G.O.; methodology: G.O., M.H., T.T., and M.Y.;

867 investigation: M.H., M.K., M.A., Md S.A.P., S.P., K.U., Md. S.H., M.Y., T.T., and G.O. (IMC
868 experiment: M.H., M.K., M.A., and G.O. IMC data analyses: M.H., M.K., Md S.A.P., K.U., and
869 G.O.; public transcriptome data analysis: Md. S.H., M.H., and S.P.; histological analysis of
870 pathological (H&E stained) specimen: M.H., M.K., K.U., and T.T.; histological analysis of IF-
871 stained specimen: M.H., M.K., K.U., G.O., and T.T.; human brain sample preparation and
872 pathological specimen: M.Y.); funding acquisition: G.O., M.Y., and M.H.; project administration:
873 G.O.; supervision: G.O.; writing—original draft: G.O.; writing—review & editing: G.O., M.H., T.T.,
874 M.K., S.P., K.U., Md. S.H., and M.Y.
875
876 **Competing interests**
877 All the other authors declare no competing interests.
878

## References


1. Feldman, E. L. et al. Amyotrophic lateral sclerosis. *Lancet* **400**, 1363–1380 (2022). doi: 10.1016/S0140-6736(22)01272-7.

2. Todd, T. W. & Petrucelli, L. Modelling amyotrophic lateral sclerosis in rodents. *Nat. Rev. Neurosci.* **23**, 231–251 (2022). doi: 10.1038/s41583-022-00564-x.

3. Xu, L. et al. Global variation in prevalence and incidence of amyotrophic lateral sclerosis: a systematic review and meta-analysis. *J. Neurol.* **267**, 944–953 (2020). doi: 10.1007/s00415-019-09652-y.

4. Ogaki, K. et al. Analysis of C9orf72 repeat expansion in 563 Japanese patients with amyotrophic lateral sclerosis. *Neurobiol. Aging* **33**, 2527.e11–2527.e16 (2012). doi: 10.1016/j.neurobiolaging.2012.05.011.

5. Hasegawa, M. et al. Phosphorylated TDP-43 in frontotemporal lobar degeneration and amyotrophic lateral sclerosis. *Ann. Neurol.* **64**, 60–70 (2008). doi: 10.1002/ana.21425.

6. Iguchi, Y. et al. Loss of TDP-43 causes age-dependent progressive motor neuron degeneration. *Brain* **136**, 1371–1382 (2013). doi: 10.1093/brain/awt029.

7. Keren-Shaul, H. et al. A unique microglia type associated with restricting development of Alzheimer's disease. *Cell* **169**, 1276–1290.e17 (2017). doi: 10.1016/j.cell.2017.05.018.

8. Mallach, A. et al. Microglia-astrocyte crosstalk in the amyloid plaque niche of an Alzheimer's disease mouse model, as revealed by spatial transcriptomics. *Cell Rep.* **43**, 114216 (2024). doi: 10.1016/j.celrep.2024.114216.

9. Liddelow, S. A. et al. Neurotoxic reactive astrocytes are induced by activated microglia. *Nature* **541**, 481–487 (2017). doi: 10.1038/nature21029.

10. Zhang, W. et al. Role of neuroinflammation in neurodegeneration development. *Signal Transduct. Target Ther.* **8**, 267 (2023). doi: 10.1038/s41392-023-01486-5.

11. Houldsworth, A. Role of oxidative stress in neurodegenerative disorders: a review of reactive oxygen species and prevention by antioxidants. *Brain Commun.* **6**, fcad356 (2024). doi: 10.1093/braincomms/fcad356.

12. Ziff, O. J. et al. Integrated transcriptome landscape of ALS identifies genome instability linked to TDP-43 pathology. *Nat. Commun.* **14**, 2176 (2023). doi: 10.1038/s41467-023-37630-6.

13. Johmura, Y. et al. Senolysis by glutaminolysis inhibition ameliorates various age-associated disorders. *Science* **371**, 265–270 (2021). doi: 10.1126/science.abb5916.

14. Yamanaka, K. et al. Astrocytes as determinants of disease progression in inherited amyotrophic lateral sclerosis. *Nat. Neurosci.* **11**, 251–253 (2008). doi: 10.1038/nn2047.

15. Yamanaka, K. & Komine, O. The multi-dimensional roles of astrocytes in ALS. *Neurosci. Res.* **126**, 31–38 (2018). doi: 10.1016/j.neures.2017.09.011.

16. Haidet-Phillips, A. M. et al. Astrocytes from familial and sporadic ALS patients are toxic to motor neurons. *Nat. Biotechnol.* **29**, 824–828 (2011). doi: 10.1038/nbt.1957.

17. Song, S. et al. Major histocompatibility complex class I molecules protect motor neurons from astrocyte-induced toxicity in amyotrophic lateral sclerosis. *Nat. Med.* **22**, 397–403 (2016). doi: 10.1038/nm.4052.

18. Ingre, C. et al. Lipids, apolipoproteins, and prognosis of amyotrophic lateral sclerosis. *Neurology* **94**, e1835–e1844 (2020). doi: 10.1212/WNL.0000000000009322.

19. Giblin, A. et al. Neuronal polyunsaturated fatty acids are protective in ALS/FTD. *Nat. Neurosci.* **28**, 737–747 (2025). doi: 10.1038/s41593-025-01889-3.

20. Ghavami, S. et al. Autophagy and apoptosis dysfunction in neurodegenerative disorders. *Prog. Neurobiol.* **112**, 24–49 (2014). doi: 10.1016/j.pneurobio.2013.10.004.

21. Neumann, M. et al. Ubiquitinated TDP-43 in frontotemporal lobar degeneration and amyotrophic lateral sclerosis. *Science* **314**, 130–133 (2006). doi: 10.1126/science.1134108.

22. Tan, C. F. et al. TDP-43 immunoreactivity in neuronal inclusions in familial amyotrophic lateral sclerosis with or without SOD1 gene mutation. *Acta Neuropathol.* **113**, 535–542 (2007). doi: 10.1007/s00401-007-0206-9.

23. Prasad, A. et al. Molecular mechanisms of TDP-43 misfolding and pathology in amyotrophic lateral sclerosis. *Front. Mol. Neurosci.* **12**, 25 (2019). doi: 10.3389/fnmol.2019.00025.

24. Cohen, T. J. et al. TDP-43 functions and pathogenic mechanisms implicated in TDP-43 proteinopathies. *Trends Mol. Med.* **17**, 659–667 (2011). doi: 10.1016/j.molmed.2011.06.004.

25. Yan, X. et al. Intra-condensate demixing of TDP-43 inside stress granules generates pathological aggregates. *Cell*, **188**, 4123–4140.e18 (2025). doi: 10.1016/j.cell.2025.04.039.

26. Urushitani, M. et al. Proteasomal inhibition by misfolded mutant superoxide dismutase 1 induces selective motor neuron death in familial amyotrophic lateral sclerosis. *J. Neurochem.* **83**, 1030–1042 (2002). doi: 10.1046/j.1471-4159.2002.01211.x.

27. Tarutani, A. et al. Ultrastructural and biochemical classification of pathogenic tau, α-synuclein and TDP-43. *Acta Neuropathol.* **143**, 613–640 (2022). doi: 10.1007/s00401-022-02426-3.

28. Braak, H. et al. Staging of brain pathology related to sporadic Parkinson's disease. *Neurobiol. Aging* **24**, 197–211 (2003). doi: 10.1016/s0197-4580(02)00065-9.

29. Jucker, M. & Walker, L. C. Self-propagation of pathogenic protein aggregates in neurodegenerative diseases. *Nature* **501**, 45–51 (2013). doi: 10.1038/nature12481.

30. Peng, C. et al. Protein transmission in neurodegenerative disease. *Nat. Rev. Neurol.* **16**, 199–212 (2020). doi: 10.1038/s41582-020-0333-7.

31. Pineda, S. S. et al. Single-cell dissection of the human motor and prefrontal cortices in ALS and FTLD. *Cell* **187**, 1971–1989.e16 (2024). doi: 10.1016/j.cell.2024.02.031.

32. Matés, J. M. et al. Glutaminase isoenzymes as key regulators in metabolic and oxidative stress against cancer. *Curr. Mol. Med.* 13, 514–534 (2013). doi: 10.2174/1566524011313040005.

33. Suzuki, S. et al. Phosphate-activated glutaminase (GLS2), a p53-inducible regulator of glutamine metabolism and reactive oxygen species. *Proc. Natl. Acad. Sci. U.S.A.* **107**, 7461–7466 (2010). doi: 10.1073/pnas.1002459107.

34. Grandke, F. et al. A single-cell atlas to map sex-specific gene-expression changes in blood upon neurodegeneration. *Nat. Commun.* **16**, 1965 (2025). doi: 10.1038/s41467-025-56833-7.

35. Pradat, P. F. The cerebellum in ALS: friend or foe? *J. Neurol. Neurosurg. Psychiatry* **92**, 1137 (2021). doi: 10.1136/jnnp-2021-327216.

36. Pereira, E. J. et al. Sporadic activation of an oxidative stress-dependent NRF2-p53 signaling network in breast epithelial spheroids and premalignancies. *Sci. Signal.* **13**, eaba4200 (2020). doi: 10.1126/scisignal.aba4200.

37. Fox, D. B. et al. NRF2 activation promotes the recurrence of dormant tumour cells through regulation of redox and nucleotide metabolism. *Nat. Metab.* **2**, 318–334 (2020). doi: 10.1038/s42255-020-0191-z.

38. Bindocci, E. et al. Three-dimensional Ca2+ imaging advances understanding of astrocyte biology. *Science* **356**, eaai8185 (2017). doi: 10.1126/science.aai8185.

39. Rothstein, J. D. et al. Decreased glutamate transport by the brain and spinal cord in amyotrophic lateral sclerosis. *N. Engl. J. Med.* **326**, 1464–1468 (1992). doi: 10.1056/NEJM199205283262204.

40. Dodge, J. C. et al. Metabolic signatures of amyotrophic lateral sclerosis reveal insights into disease pathogenesis. *Proc. Natl. Acad. Sci. U.S.A.* **110**, 10812–10817 (2013). doi: 10.1073/pnas.1308421110.

41. Zhong, L. et al. Soluble TREM2 ameliorates pathological phenotypes by modulating microglial functions in an Alzheimer's disease model. *Nat. Commun.* **10**, 1365 (2019). doi: 10.1038/s41467-019-09118-9.

42. van Lengerich, B. et al. TREM2-activating antibody with a blood-brain barrier transport vehicle enhances microglial metabolism in Alzheimer's disease models. *Nat. Neurosci.* **26**, 416–429 (2023). doi: 10.1038/s41593-022-01240-0.

43. Long, H. et al. Preclinical and first-in-human evaluation of AL002, a novel TREM2 agonistic antibody for Alzheimer's disease. *Alzheimers Res. Ther.* **16**, 235 (2024). doi: 10.1186/s13195-024-01599-1.

44. Spangenberg, E. et al. Sustained microglial depletion with CSF1R inhibitor impairs parenchymal plaque development in an Alzheimer's disease model. *Nat. Commun.* **10**, 3758 (2019). doi: 10.1038/s41467-019-11674-z.

45. Baligács, N. et al. Homeostatic microglia initially seed and activated microglia later reshape amyloid plaques in Alzheimer's Disease. *Nat. Commun.* **15**, 10634 (2024). doi: 10.1038/s41467-024-54779-w.

46. Hikosaka, M. et al. Maternal immune activation followed by peripubertal stress combinedly produce reactive microglia and confine cerebellar cognition. *Commun. Biol.* **8**, 296 (2025). doi: 10.1038/s42003-025-07566-2.

47. Wang, I. F. et al. TDP-43, the signature protein of FTLD-U, is a neuronal activity-responsive factor. *J Neurochem.* **105**, 797–806 (2008). doi: 10.1111/j.1471-4159.2007.05190.x.

48. Milanese, M. et al. Abnormal exocytotic release of glutamate in a mouse model of amyotrophic lateral sclerosis. *J. Neurochem.* **116**, 1028–1042 (2011). doi: 10.1111/j.1471-4159.2010.07155.x.

49. Bonifacino, T. et al. Altered mechanisms underlying the abnormal glutamate release in amyotrophic lateral sclerosis at a pre-symptomatic stage of the disease. *Neurobiol. Dis.* **95**, 122–133 (2016). doi: 10.1016/j.nbd.2016.07.011.

50. Okamoto, K. et al. Bunina bodies in amyotrophic lateral sclerosis. *Neuropathology* **28**, 109–115 (2008). doi: 10.1111/j.1440-1789.2007.00873.x.

51. Ma, M. et al. DAMPs and DAMP-sensing receptors in inflammation and diseases. *Immunity* **57**, 752–771 (2024). doi: 10.1016/j.immuni.2024.03.002.

52. Yu, C. H. et al. TDP-43 Triggers Mitochondrial DNA Release via mPTP to Activate cGAS/STING in ALS. *Cell* **183**, 636–649.e18 (2020). doi: 10.1016/j.cell.2020.09.020.

53. Kitamura, Y. et al. Changes of p53 in the brains of patients with Alzheimer's disease. *Biochem. Biophys. Res. Commun.* **232**, 418–421 (1997). doi: 10.1006/bbrc.1997.6301.

54. de la Monte, S. M. et al. Correlates of p53- and Fas (CD95)-mediated apoptosis in Alzheimer's disease. *J. Neurol. Sci.* **152**, 73–83 (1997). doi: 10.1016/s0022-510x(97)00131-7.

55. Mogi, M. et al. p53 protein, interferon-gamma, and NF-kappaB levels are elevated in the parkinsonian brain. *Neurosci. Lett.* **414**, 94–97 (2007). doi: 10.1016/j.neulet.2006.12.003.

56. Bae, B. I. et al. p53 mediates cellular dysfunction and behavioral abnormalities in Huntington's disease. *Neuron* **47**, 29–41 (2005). doi: 10.1016/j.neuron.2005.06.005.

57. de la Monte, S. M. et al. P53- and CD95-associated apoptosis in neurodegenerative diseases. *Lab Invest.* **78**, 401–411 (1998).

58. Martin, L. J. p53 is abnormally elevated and active in the CNS of patients with amyotrophic lateral sclerosis. *Neurobiol. Dis.* **7**(6 Pt B), 613–622 (2000). doi: 10.1006/nbdi.2000.0314.

59. Maor-Nof, M. et al. p53 is a central regulator driving neurodegeneration caused by C9orf72 poly(PR). *Cell* **184**, 689–708.e20 (2021). doi: 10.1016/j.cell.2020.12.025.

60. Cordes, J. et al. Cellular responses to RNA damage. *Cell* **188**, 885–900 (2025). doi: 10.1016/j.cell.2025.01.005.

## Figure legends

**Fig. 1 | Spatial proteomic mapping and cell-type classification in ALS tissues.**
**a**, Overview of spatially resolved single-cell proteomic profiling using Imaging Mass Cytometry (IMC) across the precentral gyrus, spinal cord, and cerebellum in individuals with sporadic ALS (sALS) and aged non-ALS controls (AC) (totaling 75,332 cells), followed by analysis of cell type features, spatial distribution, and histopathology.
**b**, Representative IMC (top) and Intercalator-Ir signal (191Ir and 193Ir) (bottom) images.
(**c**–**e**) UMAP subplots of annotated astrocyte, immune cell, excitatory neuron, inhibitory neuron, and other subtypes (others) in the precentral gyrus (**c**), spinal cord (**d**), and cerebellum (**e**).
(**f**–**n**) Characterization of annotated cell types. Heatmaps (**f**, **i**, **l**) show Z-score-scaled marker expression across cell types in the integrated sALS and AC datasets; bar plots indicate cell counts (**g**, **j**, **m**), and average cell-type proportions (mean ± SEM) (**h**, **k**, **n**) in the precentral gyrus (**f**–**h**), spinal cord (**i**–**k**), and cerebellum (**l**–**n**) of sALS and AC individuals.

**Fig. 2 | Distinct marker expression in ALS patients and spatial correlation of ALS-associated subpopulations in the motor cortices.**
**a**, Disease-related protein expression changes across cell types (ALS vs. AC). Asterisks indicate –log10(adjusted *p*-value) × effect size > 10.
**b**, Reclustering of annotated astrocyte, immune cell, and excitatory neuron populations.
**c**, Comparisons of differentially expressed proteins (DEPs) across subclassified cell types. The dot plot shows normalized expression levels derived from the reclustered data. IMC signal intensities were z-scaled across each marker for the color scale, and the mean expression level was set to 100% for circle size representation. The bottom panel shows the color scales used to define ALS-associated cell states in astrocytes, immune cells, and excitatory neurons from marker expression. Defined clusters are turquoise-squared.
**d**, Predicted transitions among ALS astrocytic subclusters indicating feature differences.
**e**, Representative IMC images of Astro_1 within a reactive gliosis lesion, as well as Immune_3, and Excit_4 cells.
**f**, Spatial distribution of ALS-associated cell subpopulations in the IMC image (left) and density contours (right). Astro_1 (red), Immune_1+3 (yellow), and Excit_4 (blue) are shown in the images.
**g**, Dot matrix plot of pairwise distance analyses. Pairwise distance among neighboring cell pairs per subcluster is compared. The color and size of the dots indicate –log10(*q*-value).
**h**,**i**, Representative H&E staining images and identification of areas rich in ALS-associated subpopulations. (**h**) Wide-field raw sample image (top), including the IMC FOV, and the corresponding H&E-stained image (bottom). (**i**) Representative gliosis images in the ALS-associated-subpopulation rich areas (1, 2) and non-gliosis in the ALS-associated-subpopulation poor area (3). Contours were overlaid on the H&E image.
**j**, Representative neurons in ALS-associated subpopulation-rich and -poor areas. Shrinkage of neuronal cell bodies with markedly eosinophilic cytoplasm was observed.
**k**, Bar graphs indicating acidification of neurons by colorimetric quantification across different areas (mean ± SEM). *p < 0.05; **$p < 0.01$, one-way ANOVA ($F(2, 237) = 5.4$) with Tukey-Kramer *post hoc* test.

**Fig. 3 | Distinct marker expression and spatial correlation of ALS-associated subpopulations in the lumbar spinal cord.**
**a**, Disease-related protein expression changes. Asterisks indicate –log10(adjusted *p*-value) × effect size > 10.
**b**, Reclustering of annotated populations of astrocytes, immune cells, and neurons.
**c**, Comparisons of differentially expressed proteins (DEPs) across subclassified cell types. The dot plot shows normalized expression levels derived from the reclustered data. IMC signal intensities were z-scaled, and the mean expression level was set to 100%. The bottom panel shows the color scales used to define ALS-associated cell states in astrocytes, immune cells, and excitatory neurons from marker expression. Defined clusters are turquoise-squared.
**d**, Representative IMC images of Astro_6 (GFAP-, pTDP-43, and GLS–positive within a reactive gliosis lesion) and Immune_3 cells.
**e**, Spatial distribution of ALS-associated cell subpopulations in the IMC image (left) and density contours (right). Astro_6 (red), Immune_3 (yellow), and Neuron_5 (blue) are shown in the images.
**f**, Dot matrix plot of pairwise distance analyses. The color and size of the dots indicate –log10(*q*-value).
**g**, Representative H&E staining images of ALS-associated-subpopulation rich and ALS-associated-subpopulation poor areas.
**h**, Eosin-based colorimetric quantification. Bar graphs (mean ± SEM) showing neuronal acidification (Red-Blue subtraction) across different areas. $^{**}p < 0.01$; $^{***}p < 0.001$, one-way ANOVA ($F(2, 93) = 28.81$) with Tukey-Kramer *post hoc* test.
**i**, A representative image of eosinophilic neurodegeneration (red arrowheads).

**Fig. 4 | Histopathology of the precentral gyrus and spinal cord.**
**a**, IMC images from the precentral gyrus and spatial distribution of ALS-related cell subpopulations. **b**, H&E-stained images of adjacent brain tissue sections. The identical field of view (FOV) as in the IMC image is overlaid with contours representing the density of ALS-associated cell clusters. Representative images in the right panels [1–3] show vascular damage, gliosis, and microglia aggregation in ALS-associated-cluster-rich areas [1, 2] and lack of gliosis in an ALS-associated-cluster-poor area [3].
**c**, Representative images of perivascular regions in ALS patient tissue and aged control (AC). Prominent gliosis was observed in ALS patient tissue (yellow circle). Coagulative necrosis (apoptotic neuronal cell bodies) was observed within blood vessels in ALS (insets) but not in AC.
**d**, Representative images of eosinophilic degeneration in spinal motor neurons. Cells containing Bunina bodies are indicated by red arrowheads. Some spinal motor neurons are degenerated (blank arrowheads). Bunina bodies are indicated by black arrows. In the right panel, a neuron with markedly acidophilic cytoplasm is shown.

**Fig. 5 | ALS-associated protein aggregation and GLS localization in human glial cells.**
**a**,**b**, Normalized fluorescence intensities of GLS-, GLS2-, and p53-specific immunostaining (confocal immunofluorescence (IF) images). Bar graphs represent pTDP-43(+) and pTDP-43(-) cells from ALS (red) and aged control (AC; blue) samples in the precentral gyrus (**a**) and spinal cord (**b**) (mean ± SEM). *$p < 0.05$, two-way ANOVA followed by Tukey-Kramer *post hoc* test with two-term Bonferroni correction.
**c**–**e**, Super-resolution microscopy images of ALS-associated protein localization in postmortem human tissues. (**c**) Z-stack images of pTDP-43 and GLS in a GFAP(+) astrocyte with its magnified view of the indicated region (yellow square). GLS protein signals colocalize with pTDP-43 aggregates in the cytoplasm. (**d**) Representative images of astrocytes co-immunostained for p53 and GLS or for pTDP-43 and GLS2, and of a neuron co-immunostained for pTDP-43 and GLS in the cytoplasm, identified with a transmitted light image and DAPI signal. (**e**) Iba1(+) microglia exhibiting pTDP-43 aggregation together with GLS expression. Our IF analyses indicate enhanced GLS and p53 immunoreactivity in subsets of microglia, astrocytes, and neurons in ALS tissues.

**Fig. 1 | Spatial proteomic mapping and cell-type classification in ALS tissues.**

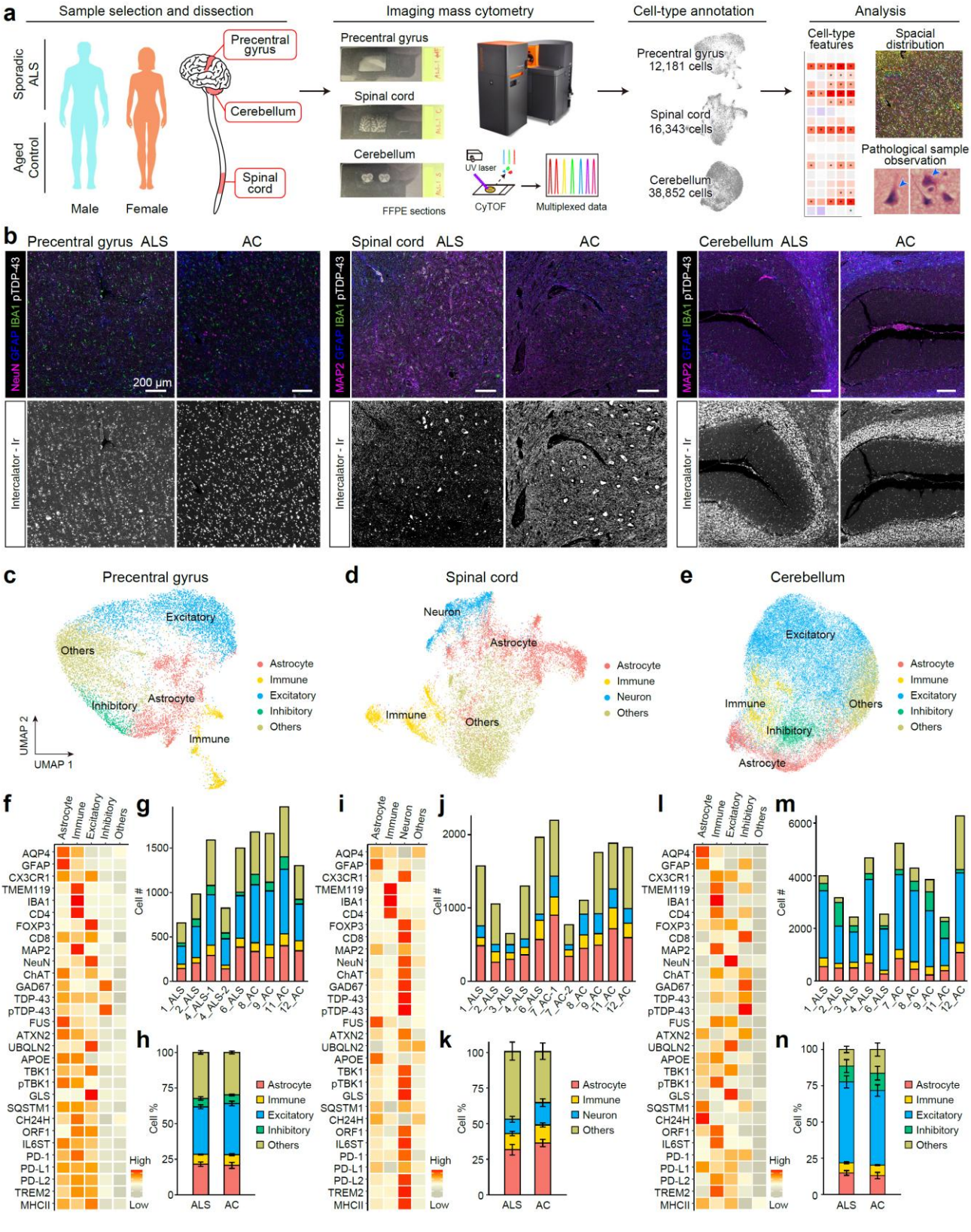


**Fig. 2 | Distinct marker expression in ALS patients and spatial correlation of ALS-associated subpopulations in the motor cortices.**

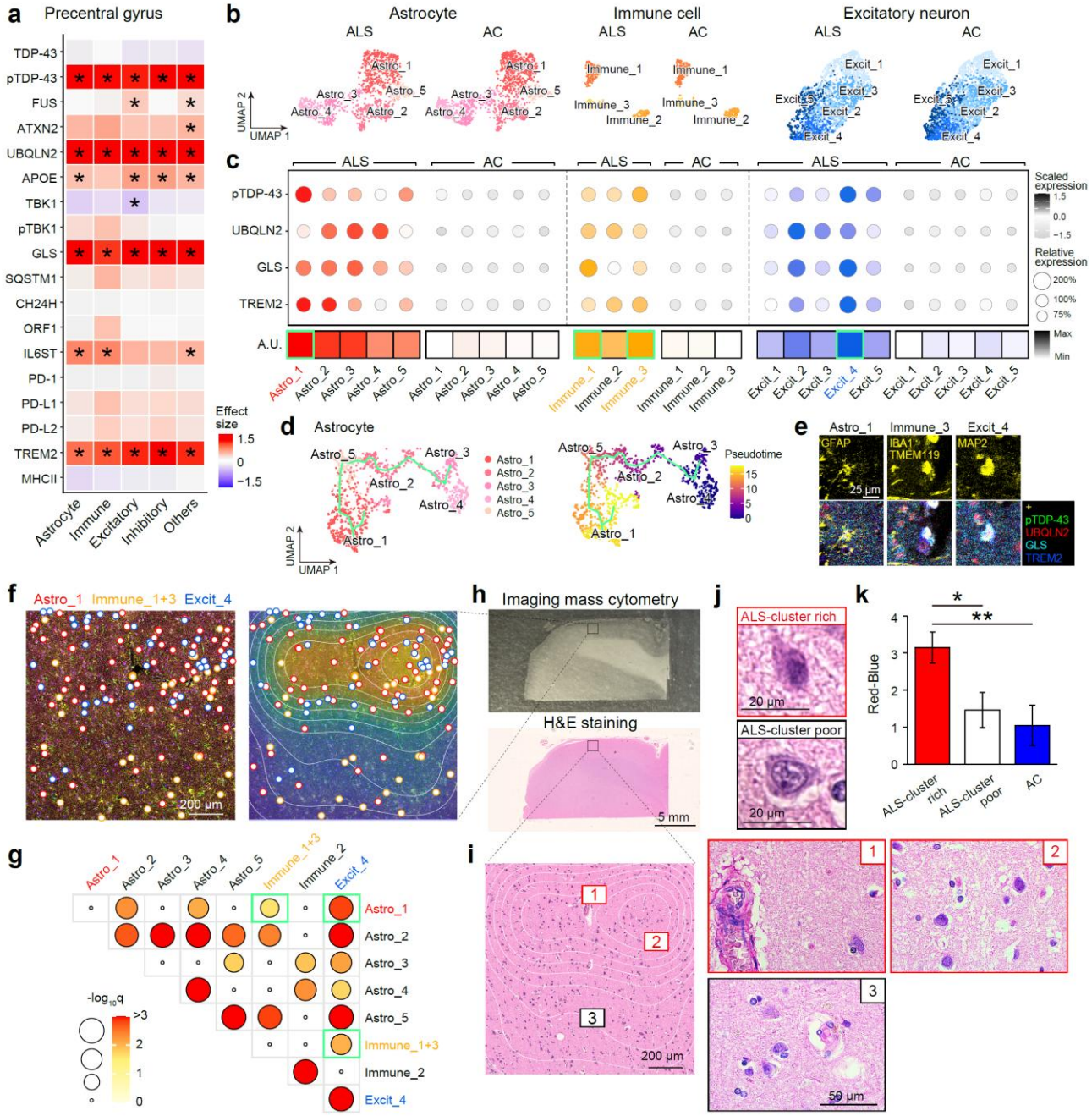


**Fig. 3 | Distinct marker expression and spatial correlation of ALS-associated subpopulations in the lumbar spinal cord.**

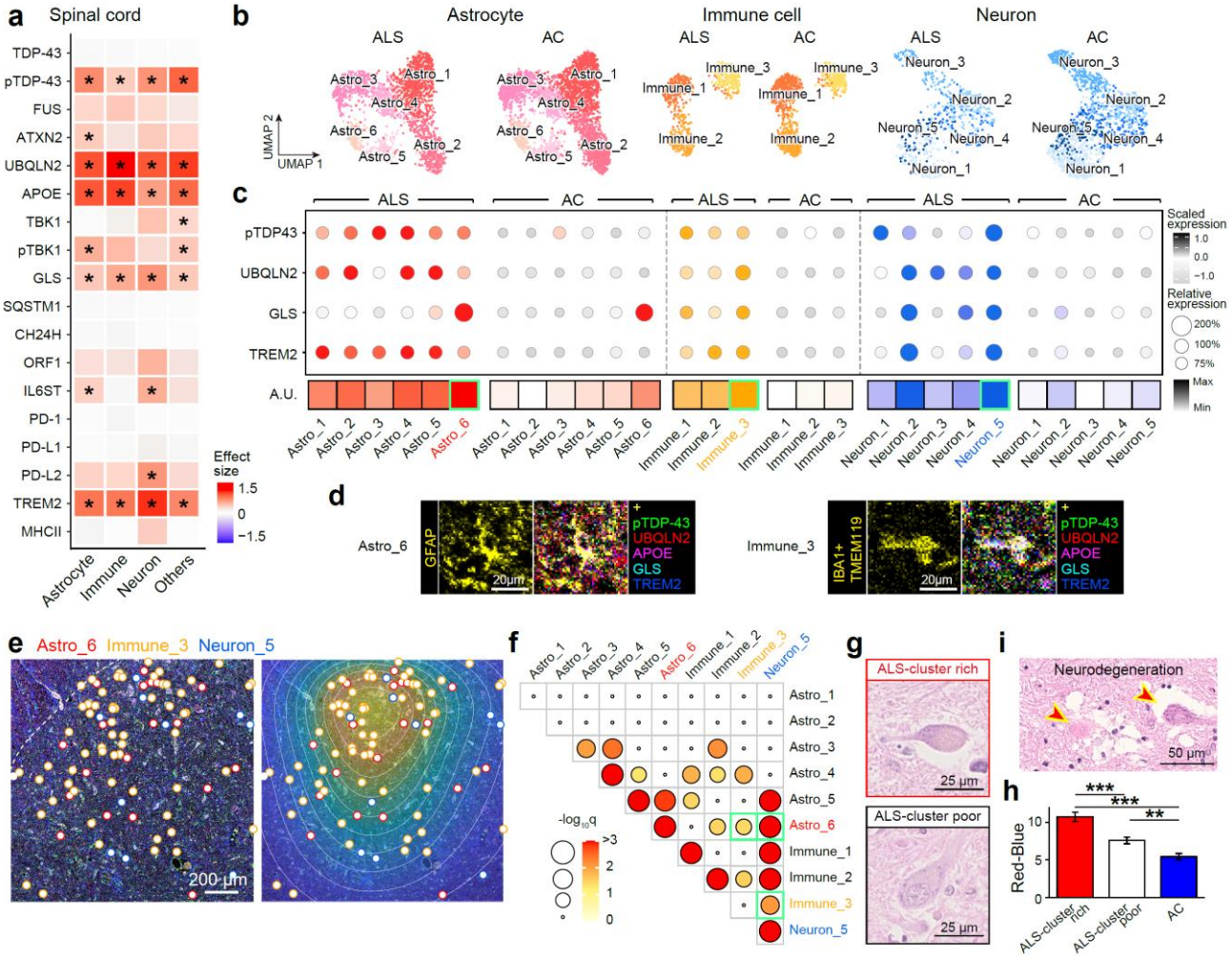


**Fig. 4 | Histopathology of the precentral gyrus and spinal cord.**

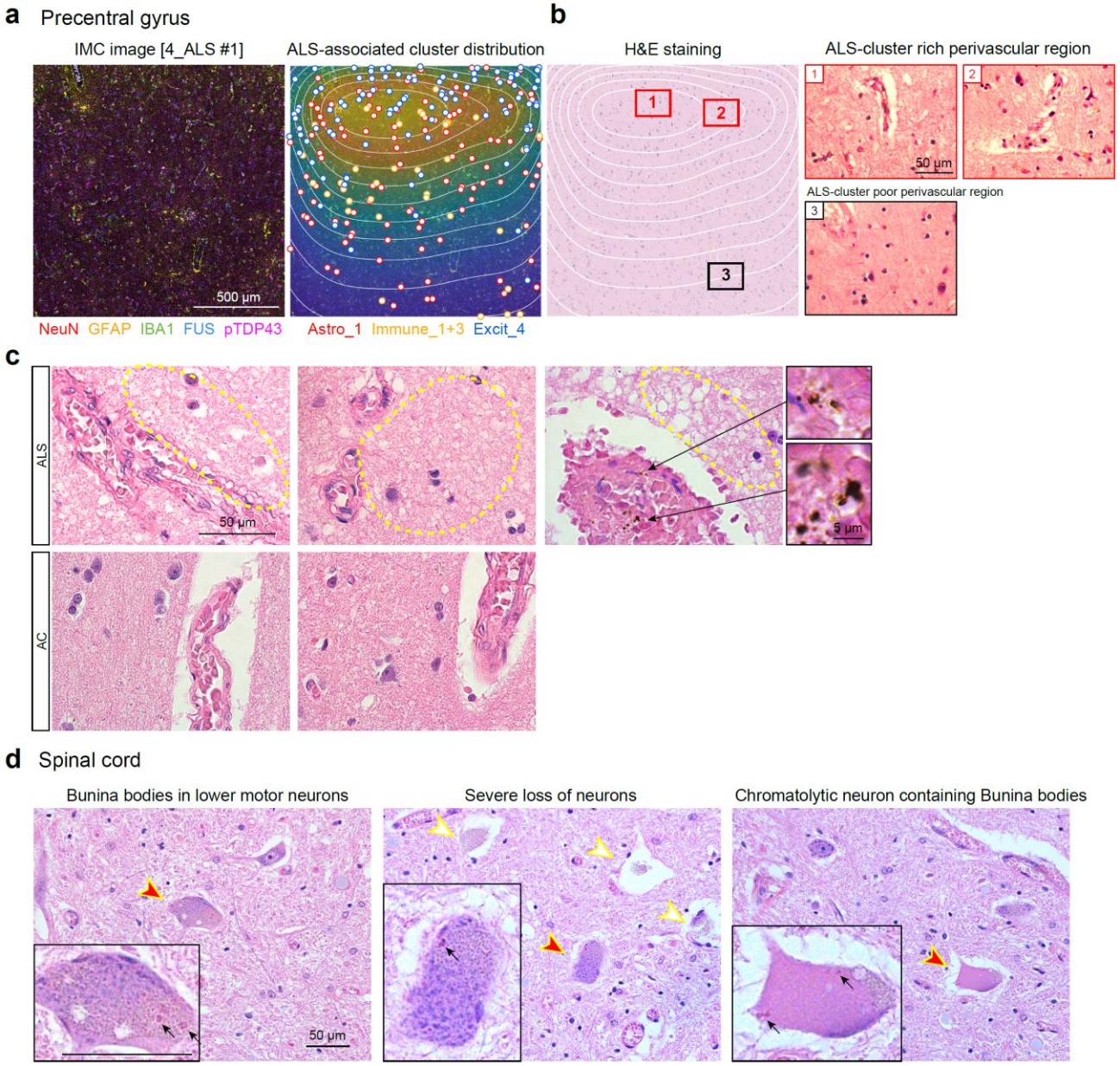
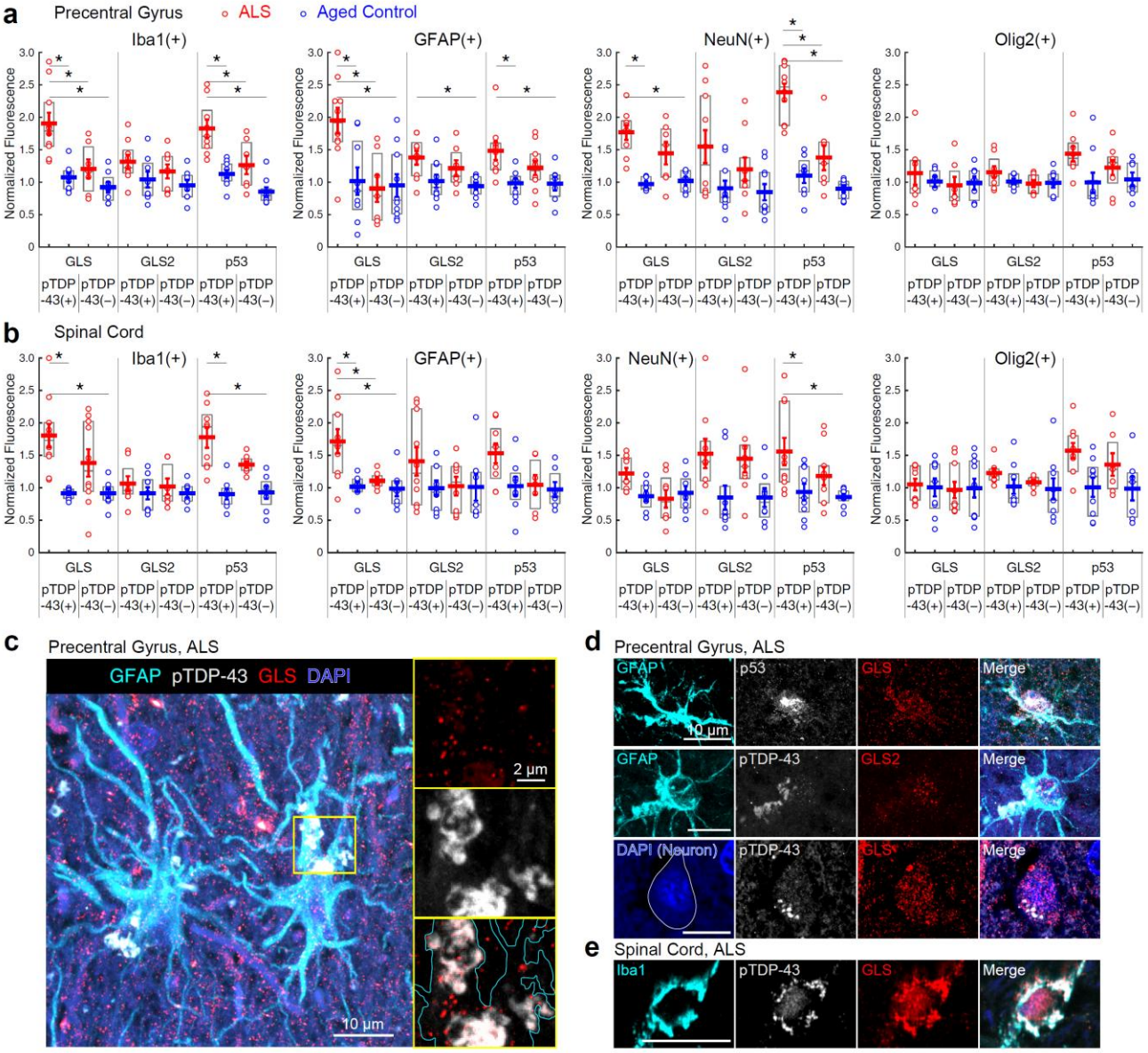


**Fig. 5 | ALS-associated protein aggregation and GLS localization in human glial cells.**



## Supplementary Files

This is a list of supplementary files associated with this preprint. Click to download.

- SupplementaryDataStatisticstableHikosakaKinoshitaetal.xlsx
- SourcedataHikosakaKinoshitaetal.xlsx
- SupplementaryInformationNCOMMS2.pdf